

Structural Insight into Redox Dynamics of Copper Bound N-Truncated Amyloid- β Peptides from *in Situ* X-ray Absorption Spectroscopy

Victor A. Streltsov,^{*,†,‡,§} Ruwini S. K. Ekanayake,[‡] Simon C. Drew,^{||} Christopher T. Chantler,[‡] and Stephen P. Best[§]

[†]Florey Department of Neuroscience and Mental Health, The University of Melbourne, Melbourne, Australia

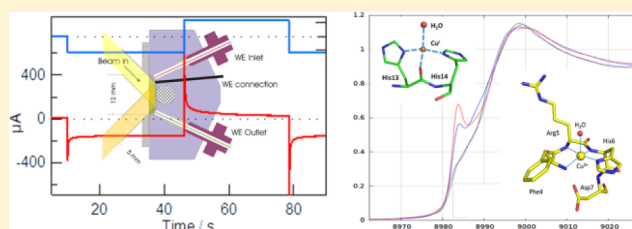
[‡]School of Physics, The University of Melbourne, Melbourne, Australia

[§]School of Chemistry, The University of Melbourne, Melbourne, Australia

^{||}Department of Medicine (Royal Melbourne Hospital), The University of Melbourne, Melbourne, Australia

S Supporting Information

ABSTRACT: X-ray absorption spectroscopy of Cu^{II} amyloid- β peptide ($A\beta$) under *in situ* electrochemical control (XAS-EC) has allowed elucidation of the redox properties of Cu^{II} bound to truncated peptide forms. The Cu binding environment is significantly different for the $A\beta_{1-16}$ and the N-truncated $A\beta_{4-9}$, $A\beta_{4-12}$, and $A\beta_{4-16}$ ($A\beta_{4-9/12/16}$) peptides, where the N-truncated sequence (F₄R₅H₆) provides the high-affinity amino-terminal copper nickel (ATCUN) binding motif. Low temperature (ca. 10 K) XAS measurements show the adoption of identical Cu^{II} ATCUN-type binding sites (Cu^{II}_{ATCUN}) by the first three amino acids (FRH) and a longer-range interaction modeled as an oxygen donor ligand, most likely water, to give a tetragonal pyramid geometry in the $A\beta_{4-9/12/16}$ peptides not previously reported. Both XAS-EC and EPR measurements show that Cu^{II}: $A\beta_{4-16}$ can be reduced at mildly reducing potentials, similar to that of Cu^{II}: $A\beta_{1-16}$. Reduction of peptides lacking the H₁₃H₁₄ residues, Cu^{II}: $A\beta_{4-9/12}$, require far more forcing conditions, with metallic copper the only metal-based reduction product. The observations suggest that reduction of Cu^{II}_{ATCUN} species at mild potentials is possible, although the rate of reduction is significantly enhanced by involvement of H₁₃H₁₄. XAS-EC analysis reveals that, following reduction, the peptide acts as a terdentate ligand to Cu^I (H₁₃, H₁₄ together with the linking amide oxygen atom). Modeling of the EXAFS is most consistent with coordination of an additional water oxygen atom to give a quasi-tetrahedral geometry. XAS-EC analysis of oxidized Cu^{II}: $A\beta_{4-12/16}$ gives structural parameters consistent with crystallographic data for a five-coordinate Cu^{III} complex and the Cu^{II}_{ATCUN} complex. The structural results suggest that Cu^{II} and the oxidation product are both accommodated in an ATCUN-like binding site.



1. INTRODUCTION

Alzheimer's disease (AD) is a progressive neurodegenerative disorder, characterized by the presence of amyloid plaques in the brain. The major constituent of AD plaques is the amyloid- β peptide ($A\beta$), which is cleaved from the membrane-bound amyloid precursor protein (APP). Further evidence for $A\beta$ involvement in AD ranges from genetic studies indicating that mutations which increase $A\beta$ production or decrease $A\beta$ clearance enhance disease progression¹ to cellular toxicity assays indicating that the $A\beta$ peptide can form neurotoxic structures.² Despite this evidence for a role for $A\beta$ in the disease state, there is no consensus on the specific forms of the peptide responsible for the pathogenesis of AD. The degree of synaptic loss correlates more with the small soluble/diffusible species of $A\beta$ oligomers,³ which in turn are in equilibrium with insoluble $A\beta$ aggregates.⁴ The current, most widely accepted theory for $A\beta$ toxicity is that small, soluble, diffusible $A\beta$ oligomers of undefined stoichiometry and composition cause synaptic damage.⁵

Recent biophysical characterization of $A\beta$ aggregates showed that the full length $A\beta_{1-42}$ peptide tends to aggregate into inert amyloid plaques in contrast to N-truncated $A\beta_{4-42}$ and pyroglutamate $A\beta_{3-42}$ ($A\beta$ pyroE₃₋₄₂) peptides, which have a higher tendency to stay soluble and maintain their toxic profile over a longer time period.^{6,7} N-terminal deletions such as $A\beta_{4-42}$ enhance generation of toxic soluble and stable $A\beta$ oligomers.⁸ The first protein sequencing studies of the amyloid plaque core (APC) from AD brains identified N-terminal heterogeneity and the majority (~64%) of the APC-AD begins with an F₄ residue corresponding to position 4 of the full 42-length sequence.^{9,10} Mass spectrometry analyses supported these findings, demonstrating that $A\beta_{4-42}$ and $A\beta_{1-42}$ are the dominant isoforms present in the hippocampus and cortex of sporadic and familial AD patients as well as in healthy controls.^{11,12}

Received: May 8, 2018

More recent studies¹³ have revealed actions of human $A\beta_{4-42}$ aggregates in the mouse brain that are consistent with a role for $A\beta_{4-42}$ in the pathogenesis of AD in humans.

There is a marked difference in the metal-binding capabilities of the N-truncated forms of $A\beta$. The predominant $A\beta_{4-42}$ peptide presents a high (femtomolar) affinity amino-terminal Cu and Ni (ATCUN) $H_2N-Xaa-Yaa-H$ sequence motif¹⁴ with $F_4R_5H_6$ residues. This enables the coordination of terminal (F_4) amine, two deprotonated backbone amides (R_5 and H_6), and the H_6 imidazole nitrogen donor atoms in a fused (S_5S_6)-membered chelate ring,¹⁵ a coordination mode inaccessible to the full-length $A\beta_{1-42}$ peptide. In this case, the first three residues (D_1 , A_2 , and E_3) along with three $H_{6/13/14}$ and Y_{10} and E_{11} residues were implicated as potential ligands in $Cu:A\beta_{1-42}$ binding, but of lower (nM) affinity.^{16–21} Involvement of either the carboxylate O (E_{11}) or imidazole N atom (H_{13} or H_{14}) or solvent coordination in the fifth site of the $Cu^{II}:ATCUN$ motif is possible and will be explored in the present study.

A *bis*-His ($H_{13}H_{14}$) motif is predominantly involved in Cu^I binding in $A\beta$ peptides.^{22–26} A role for the $H_{13}H_{14}$ motif in the reduction chemistry of $Cu:A\beta_{1-16}$ has been proposed based on the modeling of cyclic voltammetry where reduction was suggested to occur through a modified coordination site in equilibrium with the most stable geometry.²⁷ Following reduction, a subsequent equilibrium process gives Cu^I bound to the $H_{13}H_{14}$ site. Recent attempts to identify more precisely the residues needed for reduction have been based mainly on probing the effect of residue exchange on the rate of hydroxyl radical production. Those investigations suggest coordination by one H (any) and D_1 binding via the carboxyl O atom and the N-terminal amine.^{28,29} Neither the voltammetry nor the rates of hydroxyl radical production give direct structural information, and this limits the interpretation of the results, particularly when considering the impact of a change in physical conditions (e.g., pH) or of the peptide sequence. These issues will be particularly important for studies of N-truncated peptides (since D_1 plays an important role in metal binding of the full-length $A\beta$) or/and for deletion of the $H_{13}H_{14}$ motif.

ATCUN-like sequence and partial geometric features are found in ~2% of known protein structures.³⁰ Specifically, the ATCUN Cu binding site followed by *bis*-His and Y exists in Cu transporters such as the transmembrane Cu transport protein (CTR1: (1–14)MDHSHHMGMSYMS...) ³¹ as well as in human salivary antimicrobial peptides (AMP) such as histatin-5 (Hst5: DSHAKRHHGYKRKFHEKHHSHRGY).³² In these cases, the *bis*-His motif is separated by 1aa (CTR1) or 3aa (Hst5) amino acids (aa) from the ATCUN site compared to N-truncated $A\beta_{4-y}$ (6aa). A recent study³³ showed that the sequence proximity of ATCUN and *bis*-His significantly affects the chemical behavior of peptides, and those with greater spacing form stable Cu^I -peptide complexes more slowly. This $H_{13}H_{14}$ motif in N-truncated $A\beta_{4-y}$ peptide can be involved in a potential second binding site for Cu^{II} , however, with an affinity 7 orders of magnitude lower than the ATCUN binding site.¹⁴ At a substoichiometric Cu^{II} ratio, the high affinity of the ATCUN sites compete successfully with the secondary Cu^{II} binding site.¹⁴ Delineation of the role of the $H_{13}H_{14}$ site in Cu-based redox chemistry of $A\beta$ is therefore significant not only for scrutinizing the metals hypothesis of AD but more generally for Cu transport and regulation by ATCUN proteins.

One of the main and early histopathological hallmarks of AD brains is the elevated oxidative stress preceding the presence of

inflammation and amyloid plaques.³⁴ The debated metals hypothesis of AD^{35–38} proposes that oxidative stress is related to the toxicity from reactive oxygen species (ROS) produced in the brain by transition metals, primarily Cu, bound to the $A\beta$ peptide. Cell-free experiments have demonstrated that $Cu:A\beta$ complexes can be involved in Fenton chemistry to produce H_2O_2 and highly reactive OH radicals^{36,39} mediated by biological reducing agents such as ascorbate (Asc).^{36,40} ROSs initiate a variety of reactions leading to post-translational protein modifications, DNA and RNA damage, and lipid peroxidation.⁴¹ $Cu^{II}:A\beta_{4-16}$ is reported to show negligible reduction at potentials to -0.8 V vs NHE [all potentials given further in this paper are referenced to the NHE] in cyclic voltammetry measurements.¹⁴ However, indirect pathways for oxidative damage by Cu-bound ATCUN[DSH] is shown by histatin-5 (Hst5), a human salivary antimicrobial peptide (AMP). These AMPs form $Cu:ATCUN$ complexes with nuclease and protein cleavage activity. This lytic activity is proposed to be the result of oxidative damage caused by the redox cycling Cu^{II}/Cu^{III} that arises from interaction of the Cu^{II} ions with O_2 or H_2O_2 .^{32,42–44}

The present study aims to clarify the metal binding sites in the copper bound N-truncated $A\beta_{4-y}$ peptides in reducing and oxidizing environments. This should help to determine whether the copper-bound N-truncated $A\beta_{4-y}$ peptides are able to redox-cycle in a manner that might produce ROS under biologically relevant conditions. X-ray absorption spectroscopy (XAS) can deliver simultaneously structural and oxidation state information for both forms of a redox couple and play a central role in resolving questions related to the reaction path. In this investigation, methods that permit in situ XAS measurement of solutions under potentiostatic electrochemical control (XAS-EC) at ambient temperatures⁴⁵ have been applied to Cu-bound $A\beta$ peptides, including the N- and C-truncated forms ($A\beta_{x-y}$), which alter, or delete, the Cu^{II} and Cu^I binding sites. The starting structures of the Cu-bound peptides have been deduced using low temperature XAS measurements of $Cu^{II}:A\beta$ peptides as frozen solutions (ca. 10 K). The study of C-truncated peptides with $y \leq 16$ is based on their solubility relative to the full-length wild type $A\beta_{1-42}$ and $A\beta_{4-42}$ ($A\beta_{1/4-42}$) peptide.^{14,21} The metal binding residues are contained within the peptide truncated at $y = 16$ and as such are considered to be a valid model of Cu coordination and reactivity studies. The measurements were designed to (i) establish the Cu^{II} binding geometry for the high affinity sites in the $Cu:A\beta_{x-16}$ ($x = 1$ or 4), (ii) examine whether there are minor differences in binding to the ATCUN motif of N-truncated peptides, $Cu:A\beta_{4-9/12/16}$, associated with the presence of Y_{10} and E_{11} , as suggested by recent Cu^{II} pH-metric titrations,¹⁴ (iii) identify the conditions and products of reduction of the Cu^{II} -bound N-truncated peptides, $Cu:A\beta_{4-9/12/16}$, according to whether they include the *bis*- $H_{13}H_{14}$ binding site, and (iv) identify the XAS signatures for Cu^{III} so as to provide a framework for interpretation of the oxidation chemistry of $Cu^{II}:A\beta_{4-y}$. We used a novel XAS-EC method combined with uncertainty estimation to allow and inform hypothesis testing to address these critical questions.

2. EXPERIMENTAL SECTION

2.1. $A\beta$ Peptide Samples. $A\beta_{4-9/12/16}$ ($F_4RHDSG_9YEV_{12}$ -HHQK₁₆, $A\beta_{4-9/12}$ amidated) and $A\beta_{1-16}$ (DAEFRHDSGYEVHHQK) were commercially synthesized by Mimotopes (Australia) and Modpep Pty Ltd. (Melbourne, Australia), respectively, by solid-phase peptide synthesis and purified to >98% as a trifluoroacetate salt and products

verified by reverse-phase HPLC and ESI-MS. Lyophilized peptides were dissolved in deionized water with a resistivity of $18 \text{ M}\Omega \text{ cm}^{-1}$ (Millipore). The concentrations were determined using a SPECTROstar Nano UV–vis spectrometer (BMG LABETECH) with 1 cm path-length quartz cuvette, using extinction coefficients at 275 nm of $1400 \text{ M}^{-1} \text{ cm}^{-1}$ ($A\beta_{1-16}$) or $1375 \text{ M}^{-1} \text{ cm}^{-1}$ ($A\beta_{4-12/16}$) or of $16078 \text{ M}^{-1} \text{ cm}^{-1}$ at 214 nm ($A\beta_{4-9}$) using the literature method.⁴⁶

For XAS data collection, aliquots of $A\beta$ peptides were dissolved in phosphate buffer, PB (pH 7.4), then complexed with CuCl_2 as described²¹ at a Cu/peptide molar ratio of 0.9:1, with the final concentration up to 2 mM. Complexes were incubated for about 1 h at room temperature before the experiments.

For electron paramagnetic resonance (EPR) measurements, a stock solution of $^{65}\text{CuSO}_4$ was prepared by dissolving ^{65}CuO (>99%, Cambridge Isotope Laboratories) in concentrated H_2SO_4 , followed by removal of excess acid under heat and the addition of deionized water to a final concentration of 20 mM. Concentrated stock solutions of peptide and $^{65}\text{CuSO}_4$ were combined with a Cu/peptide ratio of 0.9:1 and diluted in HEPES buffer to yield final concentrations of 0.225 mM $^{65}\text{Cu}^{\text{II}}$, 0.25 mM $A\beta$, and 20 mM HEPES. The final pH was measured using a Biotrode combined glass electrode (Metrohm) and adjusted where necessary using concentrated NaOH. Solutions of 100 mM reduced glutathione (GSH) or the sodium salt of Asc, prepared fresh in deionized water and stored on ice, were then added to a final concentration of 2.5 mM.

2.2. X-ray Absorption Spectroscopy at Low Temperatures (XAS-LT). All XAS experiments were conducted at the Australian synchrotron XAS beamline (1.9 T Wiggler) with liquid nitrogen (LN_2) cooled Si (111) double crystal monochromator ($\Delta E/E$ 1.5×10^{-4}) with a Rh-coated focusing mirror to give a focused X-ray beam with a harmonic content better than 1 part in 10^5 . The incident and transmitted X-ray intensity was monitored using ionization chambers with a continuous stream of He gas. Fluorescence measurements were obtained using a 100-element LN_2 -cooled Ge detector (Canberra). Energy calibration was achieved by the simultaneous accumulation of a Cu foil spectrum (transmittance) where the inflection point of the first absorption feature was set to an energy of 8980.4 eV. Ice formation was inhibited by the addition of glycerol (~15%) to samples immediately prior to their injection into the 40 μL cavity of polycarbonate cells (2 mm \times 2 mm \times 10 mm) with Kapton (Goodfellow Cambridge, Cambridge, UK) front and back windows. Samples were frozen in LN_2 , then stored under LN_2 until transfer to the beamline closed-cycle pulse tube He cryostat (“Optisat”, Oxford Instruments). A series of Cu K-edge XAS scans up to $k = 14 \text{ \AA}^{-1}$ were obtained from samples in a fluorescence mode at 5–10 K. Radiation damage of samples was tested by quick XANES (X-ray absorption near edge spectroscopy) measurements from the same sample position with 30 min exposure intervals and also checked by comparison of the first two full EXAFS (extended X-ray absorption fine structure) spectra. The spectra recorded from each sample position were averaged to obtain the final spectra.

2.3. X-ray Absorption Spectroscopy with Electrochemical Control (XAS-EC). The XAS-EC measurements were obtained using a new flow electroynthesis cell based on an approach recently described in the literature.⁴⁵ The XAS-EC cell (Figure S1, Supporting Information) permits anaerobic handling of the solutions and minimizes the sample requirement for the measurement of XAS spectra. The working electrode (WE) consists of a $2 \times 2 \times 12 \text{ mm}^3$ reticulated vitreous carbon (RVC; 500 ppi, Desteck corporation) block in a cavity bounded by the cell body and the Kapton film window. A 6-mm-diameter RVC cylinder serves as the counter electrode (CE), and a partly oxidized polypyrrole-coated stainless-steel rod served as the reference electrode (RE).⁴⁷ The potential of this RE was +0.55 V. The RVC used for the WE and CE were made hydrophilic by immersion in concentrated H_2SO_4 followed by repeated (three to five times) washing in Milli-Q water and, finally, buffer solution. Mixing of solution between the WE and CE was minimized by packing the space with glass beads (45–60 mesh; Selby) of a diameter sufficiently large to be excluded from the cavities of the RVC electrodes. Liquid chromatography fittings were used to seal the narrow bore (0.01 in.)

1/16-in. outer-diameter Teflon tubing into the XAS-EC cell. Gas-tight syringes and fittings (Hamilton) were used to transfer solutions anaerobically, where all solutions were degassed prior to loading into the syringe. During cell operation, exclusion of air was achieved by prepurging the cell with a flow of N_2 . Solvent/supporting electrolyte was then introduced through the CE filling port while maintaining a flow of N_2 through the WE inlet port. Once full, the flow of N_2 was stopped and solvent/supporting electrolyte was collected, in turn, from the WE inlet and outlet ports.

In operation, flow of solution through the XAS-EC cell was achieved using a reciprocating pair of stepper-motor driven syringes. This avoided generation of a pressure wave which could distort the Kapton window of the XAS cell. Mass transport of the solute to the WE and minimization of sample radiation photodamage was achieved by application of a pulsed flow pattern during electrochemical reactions and throughout the collection of XAS-EC spectra. No detectable photodamage of the Cu complexes was observed at a cycle of 50:45 (forward/back) stepper motor pulses (one stepper-motor pulse displaces 0.053 μL from a 1 mL syringe). The applied potential, current, and operation of the syringe pumps were computer-controlled using locally written programs.⁴⁵ The current and potential output from the potentiostat were integrated into the data collection file for the XAS-EC measurement.

2.4. X-ray Absorption Data Processing. The XANES and EXAFS were preprocessed by the software package SAKURA⁴⁸ at the Australian synchrotron XAS beamline and also processed from the binary files for uncertainty estimations of individual data points. Inclusion of spectra from individual detector channels of the Ge fluorescence detector was based on the absence of distortions due to low sensitivity or baseline artifacts. Data points affected by monochromator glitches were also removed. The variance of the normalized fluorescence signal was used to provide a reasonable estimate of the measurement uncertainty.

For initial structural refinements, oscillations, $\chi(k)$, were extracted from the experimentally measured absorption coefficient using an automated background subtraction AUTOBK algorithm with a cubic spline fit to the data implemented in the program ATHENA.⁴⁹ Edge step normalization for each spectrum was performed by subtracting the pre-edge and post-edge backgrounds in ATHENA. The EXAFS oscillations $\chi(k)$ were quantitatively analyzed by the ARTEMIS⁴⁹ program. ATHENA and ARTEMIS are based on the IFEFFIT⁵⁰ library on numerical and XAS algorithms. Experimental data were fit to the following EXAFS function:

$$\chi(k) = S_0^2 \sum_{i=1}^{\text{shells}} \frac{N_i}{k r_i^2} F_i(k) e^{-2k^2 \sigma_i^2} e^{-2r_i/\lambda(k)} \sin[2kr_i - \varphi_i(k)]$$

The amplitude of the contribution from each coordination shell in the EXAFS function is summed to generate a fit to the data. S_0^2 is the amplitude reduction factor (core-hole factor) estimated by fitting the experimental data. N_i and r_i are the coordination number and half-path length between the central absorbing atom and a scattering atom, respectively. The mean-square disorder in the distance from the central absorbing atom to a given shell due to thermal fluctuation and structural disorder is represented by σ_i^2 and is estimated by fitting the experimental data. The photoelectron inelastic mean free path is represented by $\lambda(k)$. $F_i(k)$ is the backscattering amplitude and $\varphi_i(k)$ is the phase factor for a given coordination shell. These parameters are calculated using FEFF6.⁵¹

Restrained refinement procedures were used to minimize the number of free parameters in the least-squares refinement to increase the degree of determinacy of the model. The chemical bond distances were restrained to their values based on crystallographic structural data.⁵² Individual spectra recorded from each sample were used to obtain averaged spectra for each peptide fragment after testing for consistency and quality of the data sets. The fitting procedure consisted of successive cycles of restrained simultaneous refinements with k^1 , k^2 , and k^3 weighted $\chi(k)$ data. The final cycle of refinement was conducted with k^3 weights with $1 \leq r \leq 5$ and $3.0 \leq k \leq 12.0/10.0/11.0 \text{ \AA}^{-1}$ for XAS-LT $\text{Cu}^{\text{II}}:A\beta_{4-16}$, $\text{Cu}^{\text{II}}:A\beta_{4-12}$, and $\text{Cu}^{\text{II}}:A\beta_{4-9}$ data,

Table 1. Best Fits of EXAFS Regions of Data

complex	Cu ^{II} -Aβ _{4-9/12/16} ^a			Cu ^I -Aβ ₄₋₁₆			Cu ^{III} -Aβ _{4-12/16} ^a		
no. of data sets ^a	3			1			2		
T, K	10			298			298		
ΔE ₀ (eV)	6.33(47)			1.52(1.18)			1.62(77)		
S ₀ ²	0.950(10)			0.90(12)			0.912(91)		
r-N(Phe4) (Å) ^b	2.09(14)						2.022(26)		
r-N(Arg5) (Å)	1.958(35)						1.932(12)		
r-N(His6) (Å)	1.957(42)						1.943(89)		
r-ND1(His6) (Å)	1.966(42)						1.927(91)		
r-N(His13) (Å)				1.885(35)					
r-N(His14) (Å)				1.945(39)					
r-O(His13) (Å)				1.935(13)					
r-O(Water) (Å)	2.358(19)			2.231(29)			2.590(23)		
σ ² (Å ²) ^c	0.00351(36)			0.0068(27)			0.0020(10)		
σ _{O(His13)} ² (Å ²) ^c				0.0045(17)					
σ _w ² (Å ²)	0.0119(35)			0.0266(47) ^e			0.0163(45)		
α ^g	1.00(34)			1.25(11)			0.96(12)		
R-factor	0.029			0.036 ^d			0.029 ^e		
χ _{reduced} ²	1.052			1.257 ^d			1.066 ^e		
χ ²	52.683			65.459 ^d			53.377 ^e		
n _{ind} /n _{var.}	60/10			60/8 ^d			60/10 ^e		
F/F _{0.05} ^h	6.063/3.183			15.059/3.739			7.011/3.493		
				4.880/3.885					
ε _k	0.0015/0.0025/0.001			0.001			0.0025/0.003		

^aModel simultaneously fitted to three data sets for Aβ_{4-9/12/16} peptides complexed with Cu^{II} and to two data sets for Aβ_{4-12/16} peptides complexed with Cu^{III}. ^bThe refined structural *r* parameters are given for the first shell of N and O atoms only. ^cDisorder/thermal parameters for the first shell N and O atoms were refined only, and for higher shells these parameters were adjusted as follows: σ²(*r*_{shell} > 3.0 Å) = 2σ² (first shell); σ² (*r*_{shell} > 4.0 Å) = 2.5σ² (first shell). Fitting of the model ^dWithout the O(water) ligand. ^eWith two O(water) ligands. ^fTwo-coordinate (2N) model without O(His₁₃) and O(water) ligands. ^gα-overall scaling parameter for remaining higher shell structural *r* parameters at the final cycle of fitting. ^hF-test values calculated vs tabulated at 5% significance level as defined in the Supporting Information. ΔE₀ (eV), the refined adjustments of the photoelectron energy threshold; n_{ind}, the number of independent data points; n_{var}, the number of refined parameters; ε_k, the data uncertainty for each data set estimated from experimental errors. χ² and R factor are defined in the text; the estimated standard deviation from least-squares is given in parentheses.

respectively; 2.5 ≤ *k* ≤ 10.5 for XAS-EC Cu^I:Aβ₄₋₁₆; and 3.0 ≤ *k* ≤ 9.0/9.0 Å⁻¹ for Cu^{III}:Aβ₄₋₁₂ and Cu^{III}:Aβ₄₋₁₆ data, respectively (Table 1). The usable *k*-range in XAS-EC data is somewhat lower than accepted for the conventional experiments collected for frozen samples of higher concentrations. We should emphasize that our XAS-EC data were collected at fluorescence mode up to *k* = 14 Å⁻¹ for low concentrations (~1 mM) of flowing solution samples at room temperature. The level of noise was expectedly higher at high *k*, and therefore the data were truncated more aggressively. Extending the data range to regions in which the signal is negligible does not help to resolve transform peaks. Further optimization of the cell, solution flow, and data collection strategy should help to improve signal/noise of the data.

All multiple scattering (MS) contributions >10% and up to *l* = 4 (triple scattering paths with four legs) were included in the refined model with σ_i² values for MS paths defined from σ² parameters for single scattering paths according to the geometry of the MS paths.⁵³ Since the XANES and EXAFS regions of XAS-LT measurements for all Cu^{II}:Aβ_{4-9/12/16} (Figure 1) samples suggested that the Cu^{II} coordination geometry does not change noticeably across the samples, a multiple EXAFS data refinement has been performed. The density functional theory (DFT) optimized global model¹⁴ was used to fit simultaneously the EXAFS regions for all three Cu^{II}:Aβ_{4-9/12/16} complexes. The simultaneous refinement of the three XAS-LT (Cu^{II}:Aβ_{4-9/12/16}) to one global model allowed individual fitting of 23 structural parameters (single scattering path length up to 5 Å) with chemical bond length restraints within their standard uncertainties.⁵² The additional four parameters were overall ΔE₀ – adjustment of the photoelectron energy threshold, overall S₀², and 2 × σ_i² (Table 1). Initial values of E₀ of 8991.6, 8991.9, and 8991.4 eV for Cu^{II}:Aβ₄₋₁₆, Cu^{II}:Aβ₄₋₁₂, and Cu^{II}:Aβ₄₋₉ data, respectively, were set to the zero crossing of the second derivative nearest to the starting ATHENA/IFEFFIT's default theoretical value. In the case of one XAS-EC

Cu^I:Aβ₄₋₁₆ data set, the whole DFT optimized model³¹ was adjusted symmetrically based on the refined first-shell four structural parameters for two nitrogen and two oxygen atoms. Five additional parameters were ΔE₀ (initial E₀ = 8992.2 eV was set as described above), S₀², and 3 × σ_i² (Table 1). The refined Cu^{II}:Aβ₄₋₉ model was simultaneously fit to two XAS-EC Cu^{III}:Aβ_{4-9/12/16} data sets. The whole model was adjusted symmetrically based on the refined first-shell four structural parameters for four nitrogen and one oxygen atom. The additional four parameters were overall ΔE₀ (initial E₀ = 8993.8 eV Cu^{III}:Aβ₄₋₁₂ and E₀ = 8993.2 eV for Cu^{III}:Aβ₄₋₁₆ were set as described above), overall S₀², and 2 × σ_i² parameters (Table 1). The ΔE₀ and S₀² parameters were restrained or fixed (0.8 < S₀² < 1 and ΔE₀ = 0) at the start of the optimization and allowed to vary at the final stages of refinement along with the first shell parameters and scaling parameter, α, for the remaining structural parameters (Table 1). The data sets were weighted in ARTEMIS by the estimated average uncertainties ε_k (replacing the value of ε⁵⁴ provided by ARTEMIS) in *k*-space. The determination and extraction of standard deviations for input data points from the normalized pixel-based variance, as performed herein, is generally a far more robust estimate of ε than in the standard ARTEMIS/IFEFFIT fitting procedure. Hanning windows were used with slope parameter *dk* = 1 and *dr* = 0.1 for the forward and backward Fourier transforms, respectively. The values of the R factor and χ² (reduced goodness-of-fit) are calculated as follows⁵⁰

$$R = \frac{\sum_i^N f^2(k_i)}{\sum_i^N \chi_{\text{data}}^2(k_i)}, \chi^2 = \frac{N_{\text{ind}}}{N} \sum_i^N \frac{f^2(k_i)}{\varepsilon_k^2}, \text{ and } \chi_{\text{reduced}}^2 = \frac{N_{\text{ind}}}{N(N_{\text{ind}} - N_{\text{var}})} \sum_i^N \frac{f^2(k_i)}{\varepsilon_k^2}$$

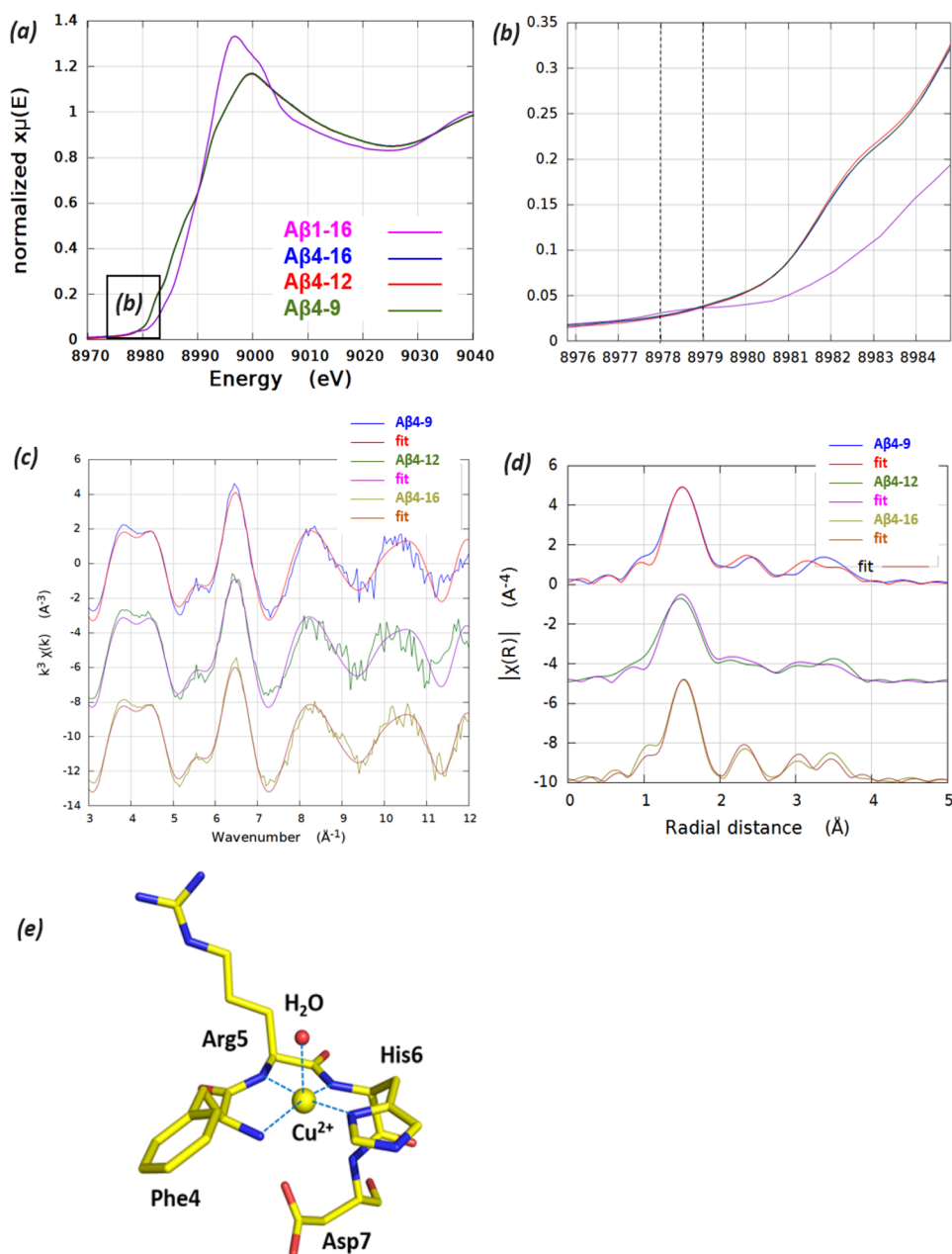


Figure 1. (a) XANES of $\text{Cu}^{\text{II}}:\text{A}\beta_{1-16}$ and $\text{Cu}^{\text{II}}:\text{A}\beta_{4-9/12/16}$ showing both the sensitivity of the XANES to the Cu coordination environment and the highly conserved geometry for the N-truncated peptides having an ATCUN sequence. (b) Pre-edge XANES region highlighting the Cu 1s-3d transitions. Analysis of the EXAFS regions for $\text{Cu}^{\text{II}}:\text{A}\beta_{4-y}$ data and simultaneous multidata fit in (c) k and (d) r space, respectively, of the DFT-optimized model of the peptide with additional axial water coordination. (e) $\text{Cu}^{\text{II}}:\text{FRHD-H}_2\text{O}$, the best fit model (EXAFS/DFT) of the ATCUN binding site for Cu^{II} in the N-truncated $\text{A}\beta_{4-y}$ peptides.

where the magnitude of the residual $f(k_i)^2 = f_{\text{xafs}}(k_i)^2 + \sum (w\Delta_{\text{restraint}}/\sigma_{\text{restraint}})^2$ with $f_{\text{xafs}}(k_i)$ defined as $f_{\text{xafs}}(k_i) = \chi_{\text{data}}(k_i) - \chi_{\text{model}}(k_i)$, where $f(k_i)$ is the minimized function which consists of the real and imaginary parts of the difference between data $\chi_{\text{data}}(k_i)$ and model $\chi_{\text{model}}(k_i)$ XAFS over the fit range k_i . The residual (penalty) function $\Delta_{\text{restraint}}$ for the restrained parameter evaluates zero if the restraint expression is satisfied or is the difference between the two sides of the restraint expression; $\sigma_{\text{restraint}}$ is the uncertainty value given for the restraint and derived here from the standard deviation of crystallographic structural parameters, and the weight w (the amplifier) determines the magnitude of the penalty. Further, N is the number of measured data points; N_{var} is the number of variables in the fit; N_{ind} is the number of independent data points, which is given by the relation $2\delta k\delta r/\pi$, with δr and δk the data ranges (max-min) in r and k space, respectively.^{55,56}

The analysis of the XAS-LT and XAS-EC experiments yielded structural information with all the refined parameters (Table 1) within the range of typical XAS parameters: the energy shift $\Delta E < 10$ eV, the amplitude reduction factor (core-hole factor) $S^2_0 \sim 0.9$ for copper compounds,⁵⁷ and thermal/disorder parameters $\sigma^2 < 0.020 \text{ \AA}^2$ being in agreement with the values obtained for similar systems.^{58,59}

2.5. EPR Spectroscopy of Chemically Reduced $\text{Cu}^{\text{II}}:\text{A}\beta$ Solutions. Immediately following addition of the reductant, samples were transferred to a quartz flat cell (Wilmad, WG-808-Q) and X-band (9.86 GHz) continuous-wave EPR spectra were obtained at room temperature (22 °C) using a Bruker Elexsys E500 spectrometer fitted with a Bruker superhigh-Q probe head (ER4122SHQE). First-harmonic EPR spectra were acquired every 10 min using the following instrumental settings: microwave power, 20 mW; magnetic field modulation amplitude, 8 G; field modulation frequency, 100 kHz; receiver time

constant, 82 ms; receiver gain, 80 dB; sweep rate, 10 gauss s^{-1} . As expected, the lineshapes show a qualitative dependence on the peptide length, with the shortest peptide giving the narrowest line shape. The spectra of $Cu^{II}:A\beta_{4-9/12/16}$ are comparable with those of the previously characterized $Cu^{II}:A\beta_{4-9}-OH$.⁶⁰ Chemical reduction of the $Cu^{II}:A\beta$ complexes by Asc and GSH was monitored by the change in intensity of the EPR signals with time. Baseline correction of all spectra was performed by weighted subtraction of the spectrum obtained using a water blank. The Cu^{II} signal was quantified using the maximum peak-to-peak intensity of the spectra. The chemical reactions were confirmed by duplicate measurements.

3. RESULTS AND DISCUSSION

3.1. XAS-LT of $Cu^{II}:A\beta$. The XANES and EXAFS regions of the low-temperature XAS of $Cu^{II}:A\beta_{4-9/12/16}$ are indistinguishable within experimental uncertainty (Figure 1a, b), suggesting that the Cu^{II} coordination geometry does not change noticeably for the three peptides. This observation is consistent with the expectation that neither Y_{10} nor E_{11} are bound to the Cu atom at pH of 7.4.¹⁴ The spectra of $Cu^{II}:A\beta_{1-16}$, while markedly different from those of the $A\beta_{4-y}$ peptides, are identical to previously measured spectra under similar conditions²¹ (Figure 1a).

3.1.1. XANES. The XANES region is sensitive to both the electronic and molecular structure of the absorber and shows that the Cu^{II} binding geometry of $Cu^{II}:A\beta_{4-9/12/16}$ is dominated by the high-affinity ATCUN site which is unaffected by residues beyond 9. The high-affinity Cu^{II} site is significantly different from that of $A\beta_{1-16}$, which has previously been shown to be highly pleomorphic and to involve from one to all three histidine residues: $H_6H_{13}H_{14}$ (Figure 1a, b).^{18,20,21,28,61} The predicted ATCUN binding site is formed by the first three residues of $Cu^{II}:A\beta_{4-y}$ peptides and appears not to involve either the carboxylate O (E_{11}) or histidine N atom (H_{13} or H_{14}) coordination in the fifth site. XANES shows the presence of a weak pre-edge peak^{21,62} at 8978 eV for $Cu^{II}:A\beta_{1-16}$, (Figures 1b and S3b) and a very weak feature at 8979 eV for $Cu^{II}:A\beta_{4-16}$ (Figures 1b and S4b), assigned to the 1s-3d electric dipole forbidden transition of Cu^{II} . The intensity of this feature has been shown to increase with the increase of the dihedral angles between ligands.⁶³ The lower intensity of the pre-edge feature of $Cu^{II}:A\beta_{4-y}$ complexes indicates a more symmetric (square planar N4) environment of the ATCUN site than in the $Cu^{II}:A\beta_{1-16}$ complex (e.g., ref 21). Similar behavior of this pre-edge peak has been observed for the ATCUN-type $Cu^{II}:DAHK$ (the N-terminal fragment of the human serum albumin) peptide complex.⁶⁴ The weak shoulder at 8987–8988 eV, which stems from either a vibronically allowed 1s-4s transition or 1s-4p transitions with a metal–ligand charge-transfer shakedown, has been assigned primarily to scattering by the axial ligands including distant (solvent) atoms, and its intensity and relative energy has been related to the number and geometry of these ligands.^{21,65} Similar features have also been observed in the XANES of $Cu^{II}:DAHK$ peptide complexes.⁶⁴

3.1.2. EXAFS. The initial three-dimensional structural model for fitting the EXAFS spectra was constructed based on the reported DFT optimized structure for the $Cu^{II}:A\beta_{4-16}$ complex.¹⁴ The first shell of Cu^{II} coordination in the ATCUN binding site of $Cu^{II}:A\beta_{4-y}$ is formed by four nitrogen ligands in equatorial positions: $N(F_4)$, the phenylalanine amino group; $N(R_5)$ and $N(H_6)$, two deprotonated amides from the first two peptide bonds; and $ND1(H_6)$, a N atom of the imidazole side chain of the histidine residue. However, the best fit was obtained with additional fifth coordination site along the apical

Jahn–Teller distortion axis occupied by O(water), analogous to the single-crystal X-ray diffraction structure of the $Cu^{II}:DAHK$ peptide complex.⁶⁴ The fit of this model to the EXAFS in k (Figure 1c) and r space (Figure 1d) and the resulting structural parameters (Table 1) reveal a good level of statistical agreement. The final EXAFS fitted structure is shown in Figure 1e. With two additional refined parameters for the water molecule, the R factor and χ^2 are decreased (Table 1) and the significance of this improvement is supported by the statistical F-test (Supporting Information), which shows that the calculated $F_{2,50} = 6.063$ value is much greater than the tabulated value of F distribution, $F_{2,50,0.05} = 3.183$, at the common significance level of 5%. The Cu^{II} ion of the $Cu^{II}:A\beta_{4-y}$ complexes is in a distorted tetragonal pyramid (penta-coordinated) environment with the distances in the range of 1.920(4)–2.07(1) Å for the equatorial atoms and 2.36(2) Å for apical water (Table 1). These values are within error estimates of the $N1-N4$ distances (1.967(2)–2.03(3) Å) and the water distance (2.565(3) Å) obtained for the $Cu^{II}:DAHK$ complex from crystallography.⁶⁴ To test if the D_7 side chain may obscure one apical coordination site (e.g., of water) as previously suggested,¹⁴ a model with the D_7 carboxyl oxygen only in the apical position instead of water was refined. The resultant fit was significantly worse (R factor and χ^2 indexes were higher for the model with an extra five parameters), and this model was rejected. The final structure agrees well with the X-ray structure of the $Cu^{II}:DAHK$ complex,⁶⁴ where the carboxyl oxygen from D_1 does not occupy the apical position. However, contrary to EXAFS analysis,⁶⁴ an attempted fit to the model including two axial oxygen atoms at similar distances resulted in nonphysically high values of $\sigma^2 > 0.02$ Å for O(water). The σ^2 parameters in Table 1 are in agreement within the errors with the values obtained by XAS for the $Cu^{II}:A\beta_{1-16}$ complex²¹ and other Cu^{II} –imidazole systems.⁶⁶

The low-temperature XAS demonstrates that all peptides in the $Cu^{II}:A\beta_{4-9/12/16}$ series coordinate Cu^{II} similarly through ATCUN-type coordination axial water oxygen in tetragonal pyramid geometry (Figure 1e). The observation of an axial water molecule indicates that other external ligands (small molecules, solvent) can occupy, transiently, this weak coordination site; for example, H_2O_2 can interact with the Cu^{II} –peptide complexes at an apical position, resulting in oxidation of Cu^{II} to Cu^{III} .⁴²

3.2. XAS-EC of $Cu^I:A\beta$, Reducing Potential. The in situ XAS-EC data of $Cu^{II}:A\beta_{1-16}$ and $Cu:A\beta_{4-9/12/16}$ have been measured at room temperature under potentiostatic control in the XAS-EC cell. The electrochemical performance of the cell was assessed using the current response to a step potential and scanning the potential (Figure S2, Supporting Information). Owing to slow electron transfer kinetics, the reduction of solutions containing $Cu^{II}:A\beta_{4-y}$ did not give a current response that was discernible from the background. Solute reduction was identified by changes in the XAS spectra, vide supra.

3.2.1. XANES. The XANES for all $Cu^{II}:A\beta$ solutions at reducing potentials (ca. -0.45 V) are shown in Figure 2a, and this is supplemented by the spectra recorded at intermediate potentials (Figures S3–S5). The spectra recorded at -0.45 V are interpreted as having near-quantitative conversion to the reduced Cu^I form. This is justified by (i) the insensitivity of the spectra to a modest change (100 mV) in potential, (ii) the flow characteristics of the experiment ensuring that there is effective contact of solution with the WE, and (iii) further reduction processes of Cu^I (to Cu^0) that can be accessed with the

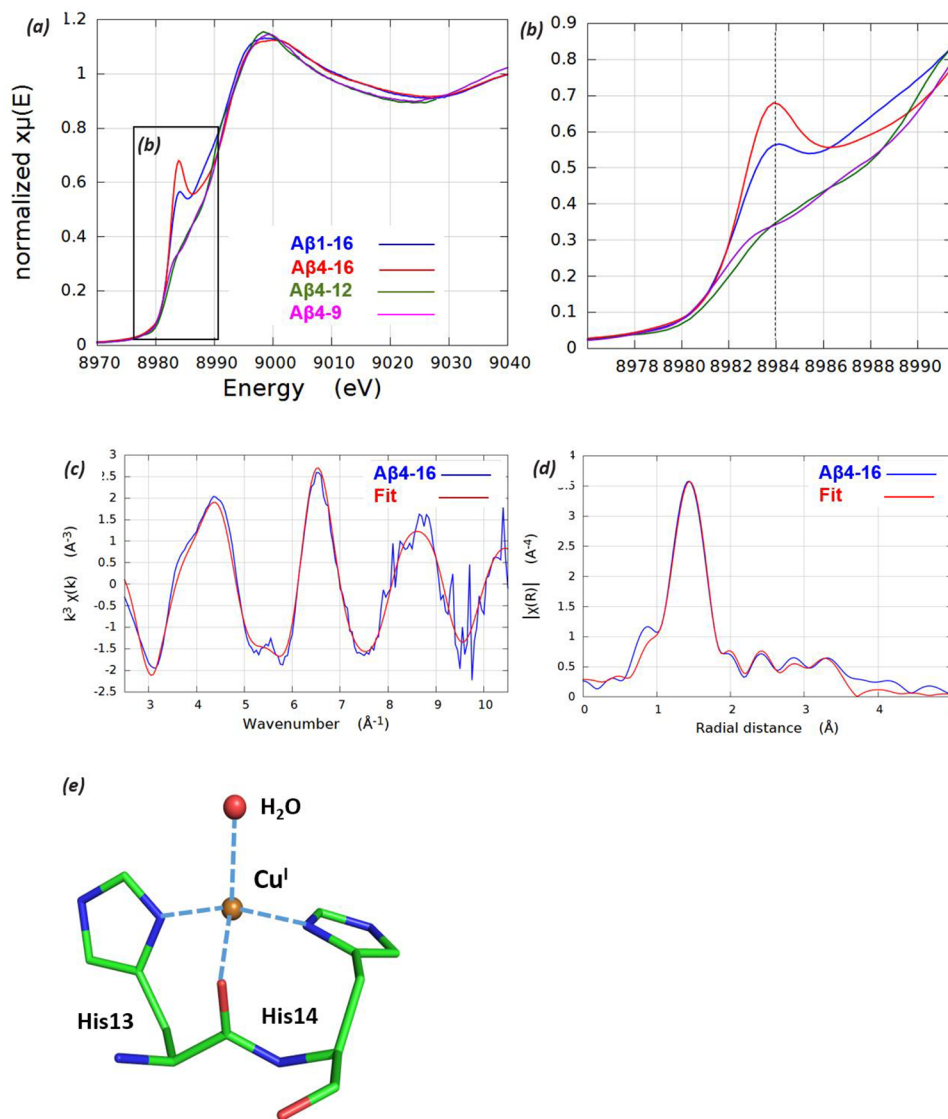


Figure 2. (a) XANES-EC near edge regions for all Cu: β peptides at a reducing potential of -0.45 V. (b) Enlarged XANES region showing Cu^{I} peaks at 8984 eV. EXAFS regions of $\text{Cu}^{\text{I}}:\text{A}\beta_{4-16}$ data with best fit of the DFT-optimized model of the *bis*-His ($\text{H}_{13}\text{H}_{14}$) site with additional axial water coordination in (c) k and (d) r space, respectively, and (e) the best fit model (EXAFS/DFT) of the $\text{H}_{13}\text{H}_{14}$ binding site for Cu^{I} in the N-truncated $\text{A}\beta_{4-16}$ peptides.

application of a much more strongly reducing potential. Importantly, reduction at these potentials does not result in significant change in the XANES spectra of the $\text{Cu}:\text{A}\beta_{4-9/12}$ complexes, indicating that even over the long time scale of the experiment (ca. 30 min) no observable reduction (electrochemical or photoinduced) was observed. These experiments show that it is not the binding of Cu^{II} to the ATCUN motif that prevents reduction of Cu but accessibility to a coordination site suitable for Cu^{I} . The spectra show the expected metal-based reduction of $\text{Cu}^{\text{II}}:\text{A}\beta_{1-16}$ but also reduction of $\text{Cu}^{\text{II}}:\text{A}\beta_{4-16}$ (Figure 2a). In both cases, the spectra exhibit a peak at ~ 8984 eV (Figure 2b and Figures S3 and S4, Supporting Information) which is attributed to the strong $1s\text{-}4p$ transition of Cu^{I} , which is known to occupy the $8980\text{--}8985$ eV region.^{40,67} The high intensity of the pre-edge peaks has been correlated with the linearity of two-coordinate Cu^{I} species.^{22–26,68} However, the peak heights in Figure 2a,b are somewhat smaller than observed before for $\text{Cu}:\text{A}\beta_{1-16}$ complexes reduced by ascorbate^{24,40} This may be an indication of incomplete reduction

of Cu^{II} with a lower intensity pre-edge peak at ~ 8984 eV.⁶⁸ A three-coordinate geometry for Cu^{I} with positions corresponding to N_{δ} (His_{13}), O (His_{13}), and N_{δ} (His_{14}) was obtained in $\text{Cu}^{\text{I}}:\text{A}\beta_{1-16}$ by first-principles molecular dynamics simulations in the Car–Parrinello scheme and this structure developed toward tetrahedral geometry during the whole simulation with possible engagement of the His_6 side chain.²³

In order to explore if the XAS-EC data could be simply explained by a mixture of Cu^{I} and Cu^{II} species previously observed in XAS-LT experiments, linear combination fitting (LCF) to the $\text{Cu}^{\text{I}}:\text{A}\beta_{4-16}$ XAS-EC data was performed using the ATHENA package. The LCF standards included our previous unpublished $\text{Cu}^{\text{I}}:\text{A}\beta_{1-16}$ XAS-LT data similar to that in ref 24 and the present $\text{Cu}^{\text{II}}:\text{A}\beta_{4-16}$ XAS-LT data. The LCF for the XANES normalized $\mu(E)$ data region was extremely unstable and sensitive to data noise with significant misfits throughout almost the entire fitting region. Alternatively, the LCF performed using EXAFS $\chi(k)$ data ($k = 3\text{--}11\text{\AA}^{-1}$) showed almost no sensitivity to data noise and converged to

the Cu^I/Cu^{II} ratio of 97:3% (Figure S6, Supporting Information). It should be noted that LCF is strongly dependent on the choice of good standards. Standards used here are from the experiments conducted at quite different conditions (low temperature and no applied voltage) and do not necessarily reproduce all features observed in in situ XAS-EC experiments. In particular, higher data noise, higher temperature (disorder), and applied voltage (atomic polarization and distortion of the electron levels) broadens and softens the pre-edge features, which can conceal the relevant contributions of oxidation state observed in standard XAS-LT experiments. Together with all other arguments presented above, it seems reasonable to assume that the Cu^I:Aβ₄₋₁₆ XAS-EC data can be modeled by a predominantly Cu^I species as EXAFS LCF may indicate. Obviously, further careful investigations should explore the completeness of Cu reduction and experimental effects on XAS-EC spectra under applied voltage and at ambient *T*, possibly using a high-energy resolution fluorescence detection approach.⁶⁹

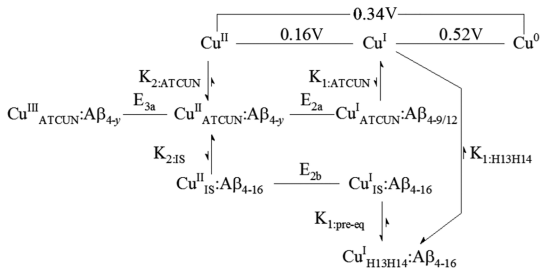
Reduction of Cu^{II}:Aβ₁₋₁₆ is proposed²⁷ to proceed through a POET (preorganization electron transfer) mechanism with relaxation of the Cu^I product to an almost linear H₁₃H₁₄ binding site. The characteristic features of the XANES spectrum for Cu^I:Aβ₁₋₁₆ were apparent following the application of mild potentials (0.05 V) and further gradual changes with the potential stepped from -0.25 to -0.65 V (Figure S3, Supporting Information). Reported pE values for Cu^{II}:Aβ₁₋₁₆/28/42 complexes are in the range of 0.28–0.34 V.^{70,71} The time frame for XAS-EC experiments is much slower than that of cyclic voltammetry where, owing to the high internal resistance of the XAS-EC cell, establishment of an equilibrium concentration of the reduced and oxidized species following a change in potential can require several tens of seconds. For Cu^{II}:Aβ₁₋₁₆, the rate of reduction depends on the time constant for the cell rather than the rate of heterogeneous electron transfer.

While not observable in conventional electrochemical measurements,¹⁴ reversible reduction of Cu^{II}:Aβ₄₋₁₆ evident in the XAS-EC experiments (Figure 1) has been observed for chemical reduction using Asc and GSH.⁷² If it is assumed that similar thermodynamic equilibrium constants apply for binding Cu^I for the Aβ₁₋₁₆ and Aβ₄₋₁₆ peptides, then the ca. 3000 times stronger binding of Cu^{II} by the ATCUN motif of the Aβ₄₋₁₆ peptide would shift $E(\text{Cu}^{\text{II/I}}:\text{A}\beta_{4-16})$ by ca. 0.21 V more negative than $E(\text{Cu}^{\text{II/I}}:\text{A}\beta_{1-16})$. Both the requirement for more forcing conditions to reduce Cu^{II}:Aβ₄₋₁₆ than Cu^{II}:Aβ₁₋₁₆ and the slow rate of reduction contribute to the potential dependence of the XANES measured for the reduction of Cu^{II}:Aβ₄₋₁₆ (Figure S4, Supporting Information). The rate of reduction is dependent on the energy difference and kinetics of the equilibrium between the ATCUN binding site and the postulated preorganization site of the POET mechanism. This intermediate site (IS) may be structurally related to the low affinity Cu^{II} binding site, which was identified in experiments with Cu^{II}/Aβ₄₋₁₆ ratios of 1.8:1.¹⁴ The structural rearrangements due to reduction or oxidation of the Cu:Aβ₄₋₁₆ complex are more dramatic than in Cu:Aβ₁₋₁₆ with potential involvement of the H₁₃H₁₄ residues separated by six residues from the initial Cu^{II}_{ATCUN} center. Furthermore, the absence of the H₁₃H₁₄ residues for the Cu^{II}:Aβ_{4-9/12} complexes has a more profound impact on reduction, which is reflected both by the potential needed for metal-based reduction to reduce Cu^{II}:Aβ_{4-9/12} and by the instability of a Cu^I product with respect to disproportionation, as evidenced by direct formation of Cu⁰ (Figure S5, Supporting Information).

3.2.2. EXAFS. XAS-EC data of Cu^{II}:Aβ₄₋₁₆ recorded at a reducing potential of -0.45 V gave XANES consistent with quantitative conversion to the reduced, Cu^I, form of the complex and were used for the structural analysis. The XANES pre-edge peaks suggest that Cu^I is bound most likely in three-coordinate geometry. Therefore, the starting model for fitting the EXAFS region of the XAS-EC data used the DFT optimized geometry³¹ for N₂O coordinated Cu^I with two imidazole δ nitrogen atoms (ND1) in a trans coordination arrangement and a carbonyl oxygen atom from H₁₃ of the peptide backbone amide between H₁₃ and H₁₄. This is analogous to one of the stable simulated models proposed for a Cu^I complex with Cu-transporter (Ctr1) N-terminal peptide Ctr1₁₋₁₄.³¹ This three-coordinate model gave reasonable fits to the experimental data, while the reduction of the model to a two-coordinate geometry with removal of the O(H₁₃) ligand significantly worsened the fit (*R* and χ^2 factors in Table 1). The preference of the three-coordinate model is supported by the statistical *F* test, which shows that the calculated $F_{2,14} = 15.059$ value is much greater than the tabulated value of *F* distribution, $F_{2,14,0.05} = 3.739$, at the significance level of 5% (Table 1). The addition of a fourth coordinating O (water) atom slightly improved the agreement between the calculated and observed EXAFS (Table 1). The significance of this improvement is supported by the *F* test that the calculated $F_{2,12} = 4.880 > F_{2,12,0.05} = 3.885$ (Table 1). However, the small difference between values suggests the addition of a water ligand to the three-coordinate model is moderately supported by the statistical accuracy of the available data. The fitting of the EXAFS of Cu^I:Aβ₄₋₁₆ data is given in Figure 2c,d. Refined parameters are given in Table 1, and the best fit model with a quasi-tetrahedral environment is depicted in Figure 2e. The final four-coordinate quasi-tetrahedral N₂O₂ center geometry for Cu^I:Aβ₄₋₁₆ is similar to the best fit obtained with a N₂OS center for Ctr1₁₋₁₄ XAS data.³¹ Analogously, the water coordination site in the Cu^I:Aβ₄₋₁₆ peptide complex can be substituted with other ligands such as the S of GSH or M₃₅ thioether (S) group, which is available in the full length of Aβ₄₋₄₂. The involvement of M₃₅ with Cu^I can be facilitated by formation of Aβ oligomeric or plaque species, and recent studies are consistent with the notion that M₃₅ of Aβ is critical to Aβ-induced neurotoxicity.⁷³⁻⁷⁵ The availability of soft donor atoms, either from an intra- or interpeptide source, can also significantly impact the kinetics of reduction—particularly for the POET mechanism where equilibrium with the kinetic in-between state precedes reduction. In this case, the conformation of the individual peptide, or tangle of peptides (oligomers), is of critical importance. This would account for the apparent difference between the ROS-generating ability of the monomeric and oligomeric forms of Aβ.

These results demonstrate clearly that, despite the near identical cyclic voltammetric response¹⁴ and binding geometry of Cu^{II} to the Aβ_{4-9/12/16} peptides, there is a marked difference in reduction chemistry for Aβ forms which incorporate the bis-His site. In this case, the reduction to a stable Cu^I form can be achieved at relatively mild potentials, albeit with a low rate of reaction. Just as for Cu^{II}:Aβ₁₋₁₆, it is likely that a POET reaction path is followed (Scheme 1) in Cu^{II}:Aβ₄₋₁₆, where the difference in kinetics results from the more stable ATCUN binding of Cu^{II}. Access to the Cu^{II/I} couple is critical for Cu homeostasis and catalytic generation of ROS. In cases where Cu binding is limited to the residues associated with the ATCUN binding site (Cu^{II}:Aβ_{4-9/12}), reduction only occurs at

Scheme 1. Modified Latimer Diagram Summarizing the Redox Chemistry of N-Truncated $A\beta$ Peptides Based on the XAS-EC and Electrochemical Studies^a



^aThe predominant component of the equilibrium is indicated by the equilibrium arrows. Under the conditions of the experiment, peptide-free Cu^I is unstable with respect to disproportionation (i.e., $E(Cu^{II/I}) < E(Cu^{I/O})$).

strongly reducing potentials and is accompanied by the deposition of Cu metal. Reoxidation of the solution in the XAS-EC cell results in quantitative reformation of the $Cu^{II}:A\beta_{4-9/12}$ complex (Scheme 1, Figure S5).

These XAS-EC experiments do not reveal the details of the pre-equilibrium IS geometry, nor the rate of electron transfer; however, transfer of Cu^{II} from the ATCUN site ($Cu^{II}_{ATCUN}:A\beta_{4-16}$) to the *bis*-His site ($Cu^{II}_{H13H14}:A\beta_{4-16}$) could reasonably proceed via H_6-H_{13}/H_{14} IS and reduction, similar to the $Cu^{II}:A\beta_{1-16}$ reduction path²⁷ (Scheme 1). In fact, an additional low affinity Cu^{II} binding site was shown to be accessible at the $Cu^{II}/A\beta_{4-16}$ ratios of 1.8:1.¹⁴ This extra binding site is most likely formed by the *bis*-His motif with additional residues, possibly including bridging H_6 . This may be facilitated by formed three (or four)-coordinate structures best fitted to the EXAFS region and manifested in the lower XANES pre-edge Cu^I peak at ~8984 eV. The lower value of K_d for $Cu^{II}_{ATCUN}:A\beta_{4-16}$ over $Cu^{II}:A\beta_{1-16}$ translates into a more negative reduction potential and a slower rate of electron transfer as reflected by the absence of an observable current response above the background for conventional voltammetry experiments.¹⁴ The rate of reduction of ATCUN-bound Cu^{II} is highly dependent on the barrier to equilibrium to the intermediate binding site(s). This has been measured in terms of the sequence separation between the *bis*-His and ATCUN sites.³³ Clearly, both the conformation and sequence of the peptide is important in the case where a single amino acid separated the two binding motifs defining the reduction properties of the Cu:protein complexes. This is further complicated in cases of peptide aggregation in the form of oligomers or plaques.

Together, these results suggest that the redox processes for ATCUN-bound Cu^{II} are highly dependent on the availability of alternate ligands and/or binding sites and the dynamic equilibria linking Cu binding to these sites.

3.3. XAS-EC of $Cu^{III}A\beta$, Oxidizing Potential. The electrochemical response of solutions of $A\beta_{4-16}$, $Cu^{II}:A\beta_{1-16}$, and $Cu^{II}:A\beta_{4-16}$ at near-neutral pH has allowed assignment of the Cu^{II} to Cu^{III} oxidation to an irreversible wave near 1.04 V.¹⁴ This process occurs at potentials near those for oxidation of uncoordinated residues Y (0.8–0.9 V), H (1.1–1.4 V), and M (1.5–1.7 V),^{76–78} complicating the assignment of metal and ligand-based redox reactions. In general, the Cu^{II} presence slightly shifts oxidation peaks to a more positive potential.⁷⁹ These problems are amenable to resolution using XAS where the XANES signatures for Cu^{II} and Cu^{III} bound to cyclic

peptides⁶² provides a framework for interpretation of the oxidation chemistry of $Cu^{II}:A\beta_{4-y}$.

3.3.1. XANES. The pre-edge XAS-EC XANES region for $Cu^{II}:A\beta_{4-y}$ ($y = 12, 16$) peptides at an oxidative potential E of 0.95–1.35 V shows changes which are consistent with the onset of an oxidation process which may be associated with the generation of Cu^{III} (Figures 3a,b and Figures S4, S5). The Y_{10} -lacking $Cu^{II}:A\beta_{4-9}$ does not show any significant changes in XAS-EC at 0.85 V which would be consistent with a Y-centered oxidation. The weak feature at 8978–8979 eV is assigned to the 1s-3d electronic transition in Cu and is a direct probe of the unfilled d orbital population.⁶² The slight shift to higher energy (~8979.5 eV, Figure 3b, also Figure S4b and S5b (Supporting Information) for $Cu^{II}:A\beta_{4-16}$ and $Cu^{II}:A\beta_{4-12}$ respectively) and small increase in the pre-edge intensity may indicate some involvement of Cu^{III} but may also reflect a change in site symmetry.

3.3.2. EXAFS. In order to examine whether the pre-edge changes are due to a change in geometry, the structure was investigated by fitting the EXAFS regions of the data sets measured at oxidative potentials of 0.95 and 1.05 V for $Cu^{III}A\beta_{4-12}$ and $Cu^{III}A\beta_{4-16}$, respectively, using the refined structure for $Cu^{II}:A\beta_{4-9/12/16}$ complexes shown in Figure 1e as a starting model (Figure 3c, d and Table 1). The best fit was obtained with ATCUN-type five-coordinate square-based pyramidal arrangement about the Cu atom with the four N atoms in the square plane unchanged, and the axial water molecule is slightly farther away from the Cu center. The F test (see SI) confirms that the addition of an axial water molecule still gives significant improvement to the fit (Table 1). The calculated value, $F_{2,20} = 7.011$ is greater than the tabulated value, $F_{2,20,0.05} = 3.493$, at a significance level of 5%. The thermal/disorder σ^2 factors are within the expected range for N ligands but lower for the O (water) atom than for Cu^{II} and Cu^I structures (Table 1), suggesting that it could be either two water molecules at similar distances coordinating Cu^{III} (Table 1) or a heavier ligand, e.g., Cl available in solution. The involvement of two deprotonated and highly polarizable backbone amides (R_5 and H_6) in the ATCUN site is important since they are able to provide sufficient electron density to stabilize high oxidation states of Cu.⁸⁰ The similarity of the EXAFS between Cu^{II} and Cu^{III} complexes indicates that the structures about the Cu center are similar in the oxidized form and allows assignment of the 8978–8789 eV feature in the XANES as a 1s-3d electronic transition of Cu, indicating significant metal contribution to the redox process. Under these circumstances, it is necessary to explain the irreversibility of the voltammetry. The XAS-LT data (section 3.1) indicate that Y_{10} is not directly involved in coordination to Cu^{II}_{ATCUN} , and this suggests that the oxidative redox chemistry would formally involve sequential redox processes, E_{p1}/E_{p2} and E_{p3} , where the equilibrium between the Cu- and Y_{10} -centered oxidation depends on the relative magnitudes of the E_{p1} and E_{p2} couples:



Here, Y_{10}^+ is a one-electron oxidized form of Y_{10} , and the oxidation corresponding to E_{p3} may be followed by rearrangement

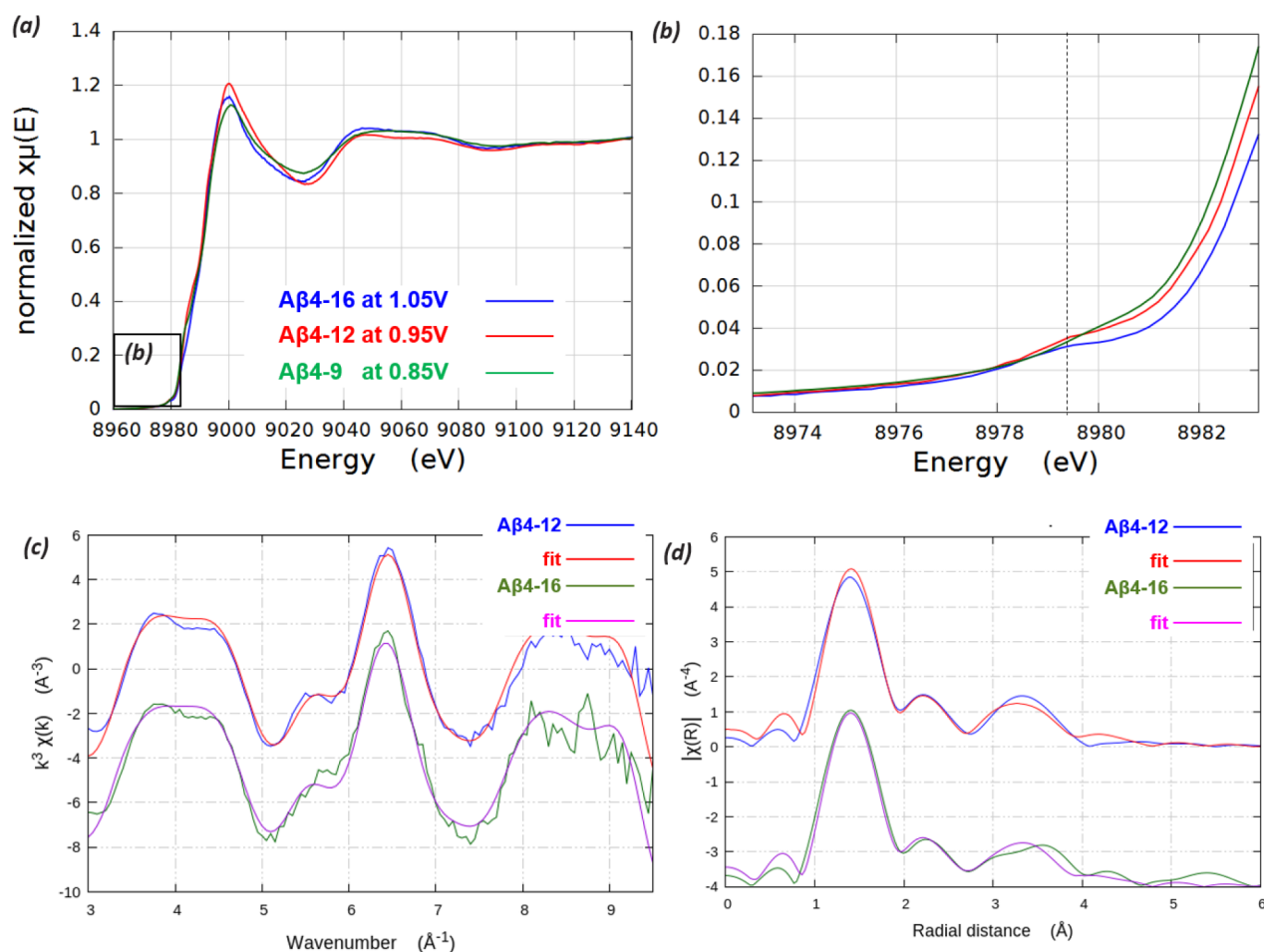


Figure 3. (a) XANES-EC near edge regions for $\text{Cu}^{\text{III}}:\text{A}\beta_{4-y}$ ($y = 12, 16$) peptides at oxidative potentials. (b) Enlarged XANES region showing Cu^{III} pre-edge peaks at ~ 8979.5 eV. Analysis of the EXAFS regions for $\text{Cu}^{\text{III}}:\text{A}\beta_{4-y}$ data ($y = 12, 16$) and simultaneous multidata fit to the ATCUN model shown in Figure 1e in (c) k and (d) r space, respectively.

and net two-electron oxidation (Y_{10}^{2+}) as summarized in the following reaction:



Analogous steps have previously been suggested for the homogeneous intramolecular electron-transfer reactions of Cu .⁷⁹ If the redox potential of the Cu -based couple (E_{p2}) is more positive ($\text{Cu}^{\text{III}}/\text{Cu}^{\text{II}} \sim 1.0$ V)⁸⁰ than that of the Y_{10} -based one (E_{p1}), then the equilibrium K_{CuY} will favor the products.

The kinetics of the Y -based redox reactions will depend on the sequence position and local environment of the Y residue.⁷⁹ This sequence of reactions would accommodate well-defined irreversible oxidation of $\text{Cu}^{\text{II}}:\text{A}\beta$ with only minor changes in the coordination environment of the Cu . It should be noted that the ATCUN Cu binding sites in CRT1 and Hst5 are also followed by Y at positions 11 and 10, respectively. The alternate interpretation, metal-centered irreversible oxidation, is unlikely, as this would require significant changes to molecular structure and significantly impact the XANES and EXAFS. Furthermore, redox activity would be expected for the Y_{10} -lacking $\text{Cu}^{\text{II}}:\text{A}\beta_{4-9}$. The slight reduction in bond length for ND1(H_6) (Table 1) may reflect the generation of Cu^{III} in an equilibrium such as that represented by K_{CuY} . Oxidation of H_6 is highly unlikely as the imidazole side chain of coordinated H is outside the range of potentials used in the experiments: 1.55 V at pH 7.⁸¹ While it is noted that the distances obtained

for the oxidized $\text{Cu}^{\text{II}}_{\text{ATCUN}}$ species agree well with crystallographic data for a five-coordinate Cu^{III} complex,⁸² these observations correlate with the potential formation of active Cu^{III} -peptide complexes (including AMPs in vivo) resulting from the oxidation of Cu^{II} by H_2O_2 , which react further to facilitate oxidative damage to the peptide.^{32,42-44} It has been proposed⁴² that further H_2O_2 molecules interact specifically at an apical position of Cu . This would correspond to the site modeled as water in the XAS-LT and XAS-EC analysis.⁷⁹ Further investigation of the potential dependence of the spectra of the different $\text{Cu}:\text{A}\beta$ complexes will be directed into characterizing this process.

3.4. EPR of $\text{Cu}^{\text{II}}_{\text{ATCUN}}:\text{A}\beta$ in the Presence of Chemical Reductants. The differing reduction chemistry of the N -truncated $\text{A}\beta_{4-y}$ peptides identified in the XAS-EC experiments should be evident in the reactions of the peptides with chemical reducing agents such as Asc and GSH. The progress of these reactions was monitored by EPR spectroscopy, where the loss of signal due to the Cu^{II} species is interpreted in terms of the formation of diamagnetic (Cu^{I}) species. Room temperature EPR measurements of $\text{Cu}:\text{A}\beta_{4-9/12/16}$ as 0.25 mM solutions with 10-fold excess of Asc ($E^0 = 0.051$ V) or GSH ($E^0 = -0.228$ V) are shown in Figure 4. With Asc as the reductant, there is no significant loss of EPR signal over a period of 24 h for $\text{Cu}:\text{A}\beta_{4-9/12}$ but a small (ca. 10%) loss of signal for $\text{Cu}:\text{A}\beta_{4-16}$ (Figure 4a). Over the same time period, the

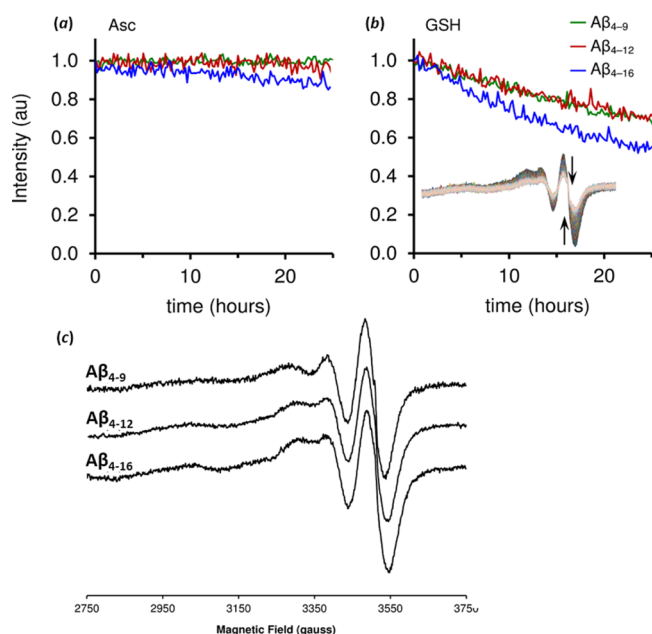


Figure 4. (a and b) Time-dependence of the EPR-active Cu^{II} signal for Cu:Aβ_{4-9/12/16} solutions in 20 mM HEPES at pH 7.4, derived from the maximum peak-to-peak intensity of the room temperature EPR spectrum. Aβ_{4-9/12/16} 0.25 mM, GSH/Asc 2.5 mM. (c) Room temperature X-band EPR spectra of Cu:Aβ_{4-9/12/16} in 20 mM HEPES at pH 7.4. Aβ_{4-9/12/16} 0.25 mM.

stronger reductant GSH effects a significant loss of the Cu^{II} signal where the rate of decay of the signal is almost 2 times higher for Cu:Aβ₄₋₁₆ than for Cu:Aβ_{4-9/12} (Figure 4b). The rate of reduction will be sensitive to the driving force for the reaction for outer-sphere electron transfer, although further work is needed to establish whether factors such as metal–ligand (Asc or GSH) binding to the metal or the peptide also make a significant contribution to the dynamics of the reaction. While the pathways of the chemical and electrochemical reductions will not necessarily be the same, it is clear that the availability of the H₁₃H₁₄ site enhances significantly the ability of the Cu^{II}_{ATCUN}:Aβ center to undergo reduction. This is a key conclusion of our XAS-EC studies of the electrochemically modulated solutions. Also consistent with the XAS-LT findings, the N-truncated Cu:Aβ_{4-9/12/16} complexes give similar EPR spectra (Figure 4c) where the peptide both provides the ATCUN binding sequence and controls access of a fifth or sixth ligand to the Cu^{II} center (Figure 4c).

4. CONCLUSIONS

XAS measurements from frozen solutions of Cu^{II}:Aβ_{4-9/12/16} complexes have been shown to have virtually identical XANES and EXAFS where this is consistent with Cu^{II}ATCUN-type binding by a regular 4N array of ligands provided by the first three amino acids (FRH). There is strong evidence for binding by a fifth, axial, ligand, which is best modeled by an oxygen atom (water) to give a tetragonal pyramidal geometry. Neither Y₁₀ nor E₁₁ give a geometry which is able to account for the fifth ligand, an observation consistent with the XAS similarity for the Cu^{II}:Aβ_{4-9/12/16} complexes. This provides support for the argument that the same high affinity ATCUN-type Cu binding site also persists for the N-truncated Aβ₄₋₄₂ peptide, a major Aβ isoform detected in AD brains.⁹

The benefits of XAS-EC measurements for complexes which undergo slow electron transfer are clearly demonstrated by the

differing reduction chemistry of Cu^{II}:Aβ_{4-9/12/16}. Whereas previous electrochemical measurements¹⁴ failed to give a response significantly different from the background for Cu^{II}:Aβ₄₋₁₆ the XAS-EC measurements demonstrate that reduction occurs at comparatively mild potentials to yield a reduced product analogous to that obtained for Cu^I:Aβ₁₋₁₆, that is, Cu^I binding by the *bis*-His (H₁₃H₁₄) binding site in a quasi-tetrahedral environment geometry. These observations show that a combination of kinetic and thermodynamic effects drive the Cu^{II/I} redox chemistry of the Cu:Aβ complexes and that this is most reasonably accommodated within the POET pathway suggested for Cu^{II}:Aβ₁₋₁₆.²⁷ Despite a more than 3 orders of magnitude higher Cu^{II} binding constant for the N-truncated peptides, redox reactions involving the Cu^I state are still accessible, where the rate of reaction depends on access to an IS geometry. For the soluble Cu^{II}:Aβ complexes, this requires involvement of the H₁₃H₁₄ residues. Since the kinetics of transfer to the *bis*-His site are very slow, the potential ROS generation by Aβ_{4-y} is not the same as that by Aβ_{1-y}. However, it is important to note that for full-length (Aβ_{x-42}), aggregated forms of the peptide, the IS may be accessed through involvement of residues from different peptides and the conformation of the interpeptide bundles, and this may lead to a spectrum of redox activities, even for the Cu^{II}_{ATCUN} forms. Being able to study IS structure during reduction by XAS-EC potentially with a high-energy resolution fluorescence detected approach⁶⁹ would be the future goal now that the Cu^{II}ATCUN and Cu^I(H₁₃H₁₄) data are at hand.

Electrochemical oxidation of Cu^{II}:Aβ_{4-12/16} may indicate the presence of mixed states of Cu^{II}/Cu^{III} bound by the ATCUN binding site with structural parameters consistent with crystallographic data for five-coordinate Cu^{III} complexes.⁸² This also includes Cu^{II}_{ATCUN}-catalyzed oxidation of residues not directly coordinated to the metal (e.g., Y₁₀ and H₁₃H₁₄). The current XAS data do not allow determination of the redox state of the oxidizable ligands not bound to the Cu.

There is some evidence that N-truncated Aβ variants represent better drug targets than full-length Aβ.⁶ Therefore, knowledge of the atomic structure of the complexes made by Cu compounds with N-truncated Aβ and their redox properties would help to understand the native function of N-truncated Aβ variants and greatly facilitate Aβ-specific therapeutic and diagnostic development. The behavior of Cu^{II}_{ATCUN}:Aβ_{4-y} has been demonstrated to be closely related to that of transmembrane Cu transport protein (CTR1), where binding to the high-affinity ATCUN[MDH] sequence with *bis*-His motif separated by 1aa allows sequestration of Cu^{II}, but a pathway for reduction to Cu^I provides a means for further chemistry (Cu release in the case of CTR1, generation of ROS for oligomeric Aβ₄₋₄₂). It remains possible that monomeric Aβ_{4-y} is a copper transfer partner or opponent for CTR1. Also, our results suggest that structural and chemical properties of N-terminal truncated peptides Aβ_{4-y} and their complexes with Cu are similar to those of antimicrobial peptides AMPs like Hst5, with the ATCUN[DSH] and *bis*-His motif separated by 3aa and Y at similar position 10, which function via modes of intracellular killing associated with inhibition of mitochondrial respiration and potentially via both transient and localized production of ROS and oxidation stress.⁴⁴ A high level of hydrogen peroxide production was observed in solutions with Hst5 and Cu, in the presence of a reductant such as Asc.⁸³ The results of chemical redox reactions^{62,84} indicate that the ability of Cu^{II}_{ATCUN}-type complexes to generate hydroxyl-like

radicals correlates with the formation of active Cu^{III} complexes in a strong oxidative environment resulting from the oxidation of Cu^I by H₂O₂, which interact with further H₂O₂. Cu:ATCUN complexes of the N-truncated forms of A β may have a similar Hst5-type mode of antimicrobial activity and may play the role of an effector molecule in the innate immune system. This could be an additional mode of the antimicrobial activity to that based on membrane binding and transmembrane pore formation.^{85,86} Our earlier structural studies⁸⁷ demonstrated that the hydrophobic part (A β _{17–42}) of A β forms dimers with striking structural similarities to dimeric forms of some human AMPs (e.g., defensins), and a recent report⁸⁸ confirmed the antimicrobial activity of A β _{1–40} in mice and *C. elegans*.

Our experiments demonstrate (1) the role that XAS can play in characterizing the electronic and molecular structure of the absorbing atom in a metalloprotein complex and that this provides the structural information needed to understand the metal chemistry of truncated peptides, (2) the viability of the strategy for the collection of solution XAS spectra from potentiostatically controlled metalloprotein/peptide samples with small sample quantities (<1 mL, 1 mM) and obtaining spectra of a quality sufficient to allow structural analysis, (3) additional insight into the path of redox reactions gained from XAS-EC methods, and (4) the possible role of less stable coordinating sites within proteins in redox/catalytic reactions. These experiments reveal a more subtle form of redox dependent metal homeostasis, which appears to be important in the chemistry of Cu:A β aggregates but must be of more general significance in the biochemistry of labile metal centers.

■ ASSOCIATED CONTENT

📄 Supporting Information

The Supporting Information is available free of charge on the ACS Publications website at DOI: 10.1021/acs.inorgchem.8b01255.

Additional experimental results of XAS-EC measurements at various redox potentials for all complexes (PDF)

■ AUTHOR INFORMATION

Corresponding Author

*E-mail: victor.streltsov@florey.edu.au.

ORCID

Victor A. Streltsov: 0000-0002-7846-4396

Stephen P. Best: 0000-0002-9399-3560

Author Contributions

The manuscript was written by V.A.S. and S.P.B. through contributions of all authors. All authors have given approval to the final version of the manuscript.

Notes

The authors declare no competing financial interest.

■ ACKNOWLEDGMENTS

We would like to acknowledge that this research was undertaken with support of the XAS beamline scientists at the Australian Synchrotron, Victoria, Australia. We would like to thank Mariuz Mital for help in preparation of samples. R.S.K.E. was supported by The Laby Foundation scholarship awarded by The School of Physics, The University of Melbourne. S.C.D. was supported by a research fellowship

awarded by the faculty of Medicine, Dentistry and Health Sciences, The University of Melbourne.

■ ABBREVIATIONS

A β , amyloid β peptide; AMP, antimicrobial peptide; Asc, ascorbate; ATCUN, amino-terminal Cu Ni binding site; CTR1, copper transport protein-1; HST5, histatin-5; DFT, density functional theory; EXAFS, extended X-ray absorption fine structure; GSH, glutathione; XANES, X-ray absorption near-edge spectroscopy; XAS-LT, X-ray absorption spectroscopy at low temperature; XAS-EC, X-ray absorption spectroscopy with electrochemical control; EPR, electron paramagnetic resonance.

■ REFERENCES

- (1) Davis, J.; Xu, F.; Miao, J.; Previti, M. L.; Romanov, G.; Ziegler, K.; Van Nostrand, W. E. Deficient cerebral clearance of vasculotropic mutant Dutch/Iowa Double A beta in human A betaPP transgenic mice. *Neurobiol. Aging* **2006**, *27* (7), 946–54.
- (2) Yankner, B. A.; Dawes, L. R.; Fisher, S.; Villa-Komaroff, L.; Oster-Granite, M. L.; Neve, R. L. Neurotoxicity of a fragment of the amyloid precursor associated with Alzheimer's disease. *Science* **1989**, *245* (4916), 417–20.
- (3) McLean, C. A.; Cherny, R. A.; Fraser, F. W.; Fuller, S. J.; Smith, M. J.; Vbeyreuther, K.; Bush, A. I.; Masters, C. L. Soluble pool of Abeta amyloid as a determinant of severity of neurodegeneration in Alzheimer's disease. *Ann. Neurol.* **1999**, *46* (6), 860–866.
- (4) Mawuenyega, K. G.; Sigurdson, W.; Ovod, V.; Munsell, L.; Kasten, T.; Morris, J. C.; Yarasheski, K. E.; Bateman, R. J. Decreased Clearance of CNS beta-Amyloid in Alzheimer's Disease. *Science* **2010**, *330* (6012), 1774–1774.
- (5) Mucke, L.; Selkoe, D. J. Neurotoxicity of amyloid beta-protein: synaptic and network dysfunction. *Cold Spring Harbor Perspect. Med.* **2012**, *2* (7), a006338.
- (6) Bayer, T. A.; Wirths, O. Immunotherapy Against N-Truncated Amyloid- β Oligomers. In *Immunotherapy and Biomarkers in Neurodegenerative Disorders*; Ingelsson, M., Lannfelt, L., Eds.' Springer New York: New York, 2016; pp 37–50.
- (7) Bayer, T. A.; Wirths, O. Focusing the amyloid cascade hypothesis on N-truncated Abeta peptides as drug targets against Alzheimer's disease. *Acta Neuropathol.* **2014**, *127* (6), 787–801.
- (8) Pike, C. J.; Overman, M. J.; Cotman, C. W. Amino-terminal Deletions Enhance Aggregation of β -Amyloid Peptides in Vitro. *J. Biol. Chem.* **1995**, *270* (41), 23895–23898.
- (9) Masters, C. L.; Simms, G.; Weinman, N. A.; Multhaup, G.; McDonald, B. L.; Beyreuther, K. Amyloid plaque core protein in Alzheimer disease and Down syndrome. *Proc. Natl. Acad. Sci. U. S. A.* **1985**, *82* (12), 4245–4249.
- (10) Masters, C. L.; Multhaup, G.; Simms, G.; Pottgiesser, J.; Martins, R. N.; Beyreuther, K. Neuronal origin of a cerebral amyloid: neurofibrillary tangles of Alzheimer's disease contain the same protein as the amyloid of plaque cores and blood vessels. *EMBO J.* **1985**, *4* (11), 2757–63.
- (11) Lewis, H.; Behr, D.; Cookson, N.; Oakley, A.; Piggott, M.; Morris, C. M.; Jaros, E.; Perry, R.; Ince, P.; Kenny, R. A.; Ballard, C. G.; Shearman, M. S.; Kalaria, R. N. Quantification of Alzheimer pathology in ageing and dementia: age-related accumulation of amyloid- β (42) peptide in vascular dementia. *Neuropathol. Appl. Neurobiol.* **2006**, *32* (2), 103–118.
- (12) Portelius, E.; Bogdanovic, N.; Gustavsson, M. K.; Volkman, I.; Brinkmalm, G.; Zetterberg, H.; Winblad, B.; Blennow, K. Mass spectrometric characterization of brain amyloid beta isoform signatures in familial and sporadic Alzheimer's disease. *Acta Neuropathol.* **2010**, *120* (2), 185–193.
- (13) Bouter, Y.; Dietrich, K.; Wittnam, J. L.; Rezaei-Ghaleh, N.; Pillot, T.; Papot-Couturier, S.; Lefebvre, T.; Sprenger, F.; Wirths, O.; Zweckstetter, M.; Bayer, T. A. N-truncated amyloid beta (Abeta) 4–

42 forms stable aggregates and induces acute and long-lasting behavioral deficits. *Acta Neuropathol.* **2013**, *126* (2), 189–205.

(14) Mital, M.; Wezynfeld, N. E.; Fraczyk, T.; Wiloch, M. Z.; Wawrzyniak, U. E.; Bonna, A.; Tumpach, C.; Barnham, K. J.; Haigh, C. L.; Bal, W.; Drew, S. C. A Functional Role for Abeta in Metal Homeostasis? N-Truncation and High-Affinity Copper Binding. *Angew. Chem., Int. Ed.* **2015**, *54* (36), 10460–4.

(15) Sovago, I.; Osz, K. Metal ion selectivity of oligopeptides. *Dalton Trans* **2006**, No. 32, 3841–54.

(16) Drew, S. C.; Masters, C. L.; Barnham, K. J. Alanine-2 carbonyl is an oxygen ligand in Cu²⁺ coordination of Alzheimer's disease amyloid-beta peptide—relevance to N-terminally truncated forms. *J. Am. Chem. Soc.* **2009**, *131* (25), 8760–8761.

(17) Stellato, F.; Menestrina, G.; Serra, M. D.; Potrich, C.; Tomazzolli, R.; Meyer-Klaucke, W.; Morante, S. Metal binding in amyloid beta-peptides shows intra- and inter-peptide coordination modes. *Eur. Biophys. J.* **2006**, *35* (4), 340–51.

(18) Karr, J. W.; Akintoye, H.; Kaupp, L. J.; Szalai, V. A. N-Terminal deletions modify the Cu²⁺ binding site in amyloid-beta. *Biochemistry* **2005**, *44* (14), 5478–87.

(19) Bousejra-ElGarah, F.; Bijani, C.; Coppel, Y.; Faller, P.; Hureau, C. Iron(II) binding to amyloid-beta, the Alzheimer's peptide. *Inorg. Chem.* **2011**, *50* (18), 9024–30.

(20) Drew, S. C.; Noble, C. J.; Masters, C. L.; Hanson, G. R.; Barnham, K. J. Pleomorphic copper coordination by Alzheimer's disease amyloid-beta peptide. *J. Am. Chem. Soc.* **2009**, *131* (3), 1195–1207.

(21) Streltsov, V.; Titmuss, S.; Epa, V.; Barnham, K.; Masters, C.; Varghese, J. The structure of the amyloid- β peptide high-affinity copper II binding site in Alzheimer disease. *Biophys. J.* **2008**, *95* (7), 3447–3456.

(22) Shin, B. K.; Saxena, S. Substantial contribution of the two imidazole rings of the His13-His14 dyad to Cu(II) binding in amyloid-beta(1–16) at physiological pH and its significance. *J. Phys. Chem. A* **2011**, *115* (34), 9590–9602.

(23) Furlan, S.; Hureau, C.; Faller, P.; La Penna, G. Modeling the Cu⁺ binding in the 1–16 region of the amyloid-beta peptide involved in Alzheimer's disease. *J. Phys. Chem. B* **2010**, *114* (46), 15119–33.

(24) Hureau, C.; Balland, V.; Coppel, Y.; Solari, P. L.; Fonda, E.; Faller, P. Importance of dynamical processes in the coordination chemistry and redox conversion of copper amyloid-beta complexes. *J. Biol. Inorg. Chem.* **2009**, *14* (7), 995–1000.

(25) Himes, R. A.; Park, G. Y.; Siluvai, G. S.; Blackburn, N. J.; Karlin, K. D. Structural studies of copper(I) complexes of amyloid-beta peptide fragments: formation of two-coordinate bis(histidine) complexes. *Angew. Chem., Int. Ed.* **2008**, *47* (47), 9084–7.

(26) Shearer, J.; Szalai, V. A. The amyloid-beta peptide of Alzheimer's disease binds Cu(I) in a linear bis-his coordination environment: insight into a possible neuroprotective mechanism for the amyloid-beta peptide. *J. Am. Chem. Soc.* **2008**, *130* (52), 17826–35.

(27) Balland, V.; Hureau, C.; Savéant, J.-M. Electrochemical and homogeneous electron transfers to the Alzheimer amyloid- β copper complex follow a preorganization mechanism. *Proc. Natl. Acad. Sci. U. S. A.* **2010**, *107* (40), 17113–17118.

(28) Cheignon, C.; Jones, M.; Atrian-Blasco, E.; Kieffer, I.; Faller, P.; Collin, F.; Hureau, C. Identification of key structural features of the elusive Cu-A[small beta] complex that generates ROS in Alzheimer's disease. *Chemical Science* **2017**, *8* (7), 5107–5118.

(29) Atrián-Blasco, E.; del Barrio, M.; Faller, P.; Hureau, C. Ascorbate Oxidation by Cu(Amyloid- β) Complexes: Determination of the Intrinsic Rate as a Function of Alterations in the Peptide Sequence Revealing Key Residues for Reactive Oxygen Species Production. *Anal. Chem.* **2018**, *90*, 5909.

(30) Sankararamakrishnan, R.; Verma, S.; Kumar, S. ATCUN-like metal-binding motifs in proteins: identification and characterization by crystal structure and sequence analysis. *Proteins: Struct., Funct., Genet.* **2005**, *58* (1), 211–21.

(31) Pushie, M. J.; Shaw, K.; Franz, K. J.; Shearer, J.; Haas, K. L. Model Peptide Studies Reveal a Mixed Histidine-Methionine Cu(I)

Binding Site at the N-Terminus of Human Copper Transporter 1. *Inorg. Chem.* **2015**, *54* (17), 8544–8551.

(32) Tay, W. M.; Hanafy, A. I.; Angerhofer, A.; Ming, L. J. A plausible role of salivary copper in antimicrobial activity of histatin-5—metal binding and oxidative activity of its copper complex. *Bioorg. Med. Chem. Lett.* **2009**, *19* (23), 6709–12.

(33) Schwab, S.; Shearer, J.; Conklin, S. E.; Alies, B.; Haas, K. L. Sequence proximity between Cu(II) and Cu(I) binding sites of human copper transporter 1 model peptides defines reactivity with ascorbate and O₂. *J. Inorg. Biochem.* **2016**, *158*, 70–76.

(34) Smith, M. A.; Nunomura, A.; Zhu, X.; Takeda, A.; Perry, G. Metabolic, Metallic, and Mitotic Sources of Oxidative Stress in Alzheimer Disease. *Antioxid. Redox Signaling* **2000**, *2* (3), 413–420.

(35) Bush, A. I. The metallobiology of Alzheimer's disease. *Trends Neurosci.* **2003**, *26* (4), 207–214 and references therein.

(36) Barnham, K. J.; Masters, C. L.; Bush, A. I. Neurodegenerative diseases and oxidative stress. *Nat. Rev. Drug Discovery* **2004**, *3* (3), 205–214 and references therein.

(37) Ganguly, G.; Chakrabarti, S.; Chatterjee, U.; Saso, L. Proteinopathy, oxidative stress and mitochondrial dysfunction: cross talk in Alzheimer's disease and Parkinson's disease. *Drug Des., Dev. Ther.* **2017**, *11*, 797–810.

(38) Drew, S. C. The Case for Abandoning Therapeutic Chelation of Copper Ions in Alzheimer's Disease. *Front. Neurosci.* **2017**, *11*, 317 DOI: 10.3389/fnins.2017.00317.

(39) Smith, D. G.; Cappai, R.; Barnham, K. J. The redox chemistry of the Alzheimer's disease amyloid beta peptide. *Biochim. Biophys. Acta, Biomembr.* **2007**, *1768* (8), 1976–1990.

(40) Streltsov, V. A.; Varghese, J. N. Substrate mediated reduction of copper-amyloid- β complex in Alzheimer's disease. *Chem. Commun.* **2008**, No. 27, 3169–3171.

(41) Markesbery, W. R.; Lovell, M. A. Damage to lipids, proteins, dna, and rna in mild cognitive impairment. *Arch. Neurol.* **2007**, *64* (7), 954–956.

(42) Kaczmarek, P.; Jezowska-Bojczuk, M.; Gatner, K.; Bal, W. Oxidative reactivity of Cu-TESHMK- and its alanine analogues. *Dalton Trans* **2005**, No. 11, 1985–8.

(43) Burke, S. K.; Xu, Y.; Margerum, D. W. Cu(II)Gly²HisGly oxidation by H₂O₂/ascorbic acid to the Cu(III) complex and its subsequent decay to alkene peptides. *Inorg. Chem.* **2003**, *42* (19), 5807–17.

(44) Puri, S.; Edgerton, M. How does it kill?: understanding the candidal mechanism of salivary histatin 5. *Eukaryotic Cell* **2014**, *13* (8), 958–64.

(45) Best, S. P.; Levina, A.; Glover, C.; Johannessen, B.; Kappen, P.; Lay, P. A. XAS spectroelectrochemistry: reliable measurement of X-ray absorption spectra from redox manipulated solutions at room temperature. *J. Synchrotron Radiat.* **2016**, *23* (3), 743–750.

(46) Kuipers, B. J. H.; Gruppen, H. Prediction of Molar Extinction Coefficients of Proteins and Peptides Using UV Absorption of the Constituent Amino Acids at 214 nm To Enable Quantitative Reverse Phase High-Performance Liquid Chromatography–Mass Spectrometry Analysis. *J. Agric. Food Chem.* **2007**, *55* (14), 5445–5451.

(47) Ghilane, J.; Hapiot, P.; Bard, A. J. Metal/Polypyrrrole Quasi-Reference Electrode for Voltammetry in Nonaqueous and Aqueous Solutions. *Anal. Chem.* **2006**, *78* (19), 6868–6872.

(48) Kappen, P.; Ruben, G.; Moll, A. *Sakura, a tool to pre-process fluorescence XAS data from multi-pixel detectors*; The Australian Synchrotron, 2015.

(49) Ravel, B.; Newville, M. ATHENA, ARTEMIS, HEPHAESTUS: data analysis for X-ray absorption spectroscopy using IFEFFIT. *J. Synchrotron Radiat.* **2005**, *12* (4), 537–41.

(50) Newville, M. IFEFFIT: interactive XAFS analysis and FEFF fitting. *J. Synchrotron Radiat.* **2001**, *8* (2), 322–324.

(51) Zabinsky, S. I.; Rehr, J. J.; Ankudinov, A.; Albers, R. C.; Eller, M. J. Multiple-scattering calculations of x-ray-absorption spectra. *Phys. Rev. B: Condens. Matter Mater. Phys.* **1995**, *52* (4), 2995–3009.

- (52) Engh, R. A.; Huber, R. Accurate bond and angle parameters for X-ray protein structure refinement. *Acta Crystallogr., Sect. A: Found. Crystallogr.* **1991**, *47* (4), 392–400.
- (53) Hudson, E. A.; Allen, P. G.; Terminello, L. J.; Denecke, M. A.; Reich, T. Polarized x-ray-absorption spectroscopy of the uranyl ion: Comparison of experiment and theory. *Phys. Rev. B: Condens. Matter Mater. Phys.* **1996**, *54* (1), 156–165.
- (54) Newville, M.; Boyanov, B. I.; Sayers, D. E. Estimation of measurement uncertainties in XAFS data. *J. Synchrotron Radiat.* **1999**, *6* (3), 264–265.
- (55) Lee, P. A.; Citrin, P. H.; Eisenberger, P.; Kincaid, B. M. Extended x-ray absorption fine structure - its strengths and limitations as a structural tool. *Rev. Mod. Phys.* **1981**, *53* (4), 769–806.
- (56) Stern, E. A. Number of relevant independent points in x-ray-absorption fine-structure spectra. *Phys. Rev. B: Condens. Matter Mater. Phys.* **1993**, *48* (13), 9825–9827.
- (57) Levina, A.; Armstrong, R. S.; Lay, P. A. Three-dimensional structure determination using multiple-scattering analysis of XAFS: applications to metalloproteins and coordination chemistry. *Coord. Chem. Rev.* **2005**, *249* (1–2), 141–160.
- (58) Poiarkova, A. V.; Rehr, J. J. Multiple-scattering x-ray-absorption fine-structure Debye-Waller factor calculations. *Phys. Rev. B: Condens. Matter Mater. Phys.* **1999**, *59* (2), 948–957.
- (59) Dimakis, N.; Bunker, G. Group-fitted ab initio single- and multiple-scattering EXAFS Debye-Waller factors. *Phys. Rev. B: Condens. Matter Mater. Phys.* **2002**, *65* (20), 201103.
- (60) Mital, M.; Bal, W.; Fraczyk, T.; Drew, S. C. Interplay between Copper, Nephrilysin, and N-Truncation of β -Amyloid. *Inorg. Chem.* **2018**, *57* (11), 6193–6197.
- (61) Yu, H.; Ren, J.; Qu, X. Different hydration changes accompanying copper and zinc binding to amyloid beta-peptide: water contribution to metal binding. *ChemBioChem* **2008**, *9* (6), 879–82.
- (62) Pratesi, A.; Giulii, G.; Cicconi, M. R.; Della Longa, S.; Weng, T. C.; Ginanneschi, M. Dioxygen Oxidation Cu(II) \rightarrow Cu(III) in the Copper Complex of cyclo(Lys-DHis-beta Ala-His): A Case Study by EXAFS and XANES Approach. *Inorg. Chem.* **2012**, *51* (15), 7969–7976.
- (63) Sano, M.; Komorita, S.; Yamatera, H. XANES spectra of copper(II) complexes: correlation of the intensity of the $1s_{\text{fwd}}^{\text{darw}}$ 3d transition and the shape of the complex. *Inorg. Chem.* **1992**, *31* (3), 459–463.
- (64) Hureau, C.; Eury, H.; Guillot, R.; Bijani, C.; Sayen, S.; Solari, P.-L.; Guillon, E.; Faller, P.; Dorlet, P. X-ray and Solution Structures of CuIIHGK and CuIIDAHK Complexes: Influence on Their Redox Properties. *Chem. - Eur. J.* **2011**, *17* (36), 10151–10160.
- (65) Strange, R. W.; Alagna, L.; Durham, P.; Hasnain, S. S. An understanding of the X-ray absorption near-edge structure of copper(II) imidazole complexes. *J. Am. Chem. Soc.* **1990**, *112* (11), 4265–4268.
- (66) Binsted, N.; Strange, R. W.; Hasnain, S. S. Constrained and restrained refinement in EXAFS data analysis with curved wave theory. *Biochemistry* **1992**, *31* (48), 12117–25.
- (67) Kau, L. S.; Spira-Solomon, D. J.; Penner-Hahn, J. E.; Hodgson, K. O.; Solomon, E. I. X-ray absorption edge determination of the oxidation state and coordination number of copper. Application to the type 3 site in *Rhus vernicifera* laccase and its reaction with oxygen. *J. Am. Chem. Soc.* **1987**, *109* (21), 6433–6442.
- (68) Himes, R. A.; Park, G. Y.; Barry, A. N.; Blackburn, N. J.; Karlin, K. D. Synthesis and X-ray absorption spectroscopy structural studies of Cu(I) complexes of histidylhistidine peptides: the predominance of linear 2-coordinate geometry. *J. Am. Chem. Soc.* **2007**, *129* (17), 5352–3.
- (69) Vollmers, N. J.; Müller, P.; Hoffmann, A.; Herres-Pawlis, S.; Rohrmüller, M.; Schmidt, W. G.; Gerstmann, U.; Bauer, M. Experimental and Theoretical High-Energy-Resolution X-ray Absorption Spectroscopy: Implications for the Investigation of the Entatic State. *Inorg. Chem.* **2016**, *55* (22), 11694–11706.
- (70) Guilloureau, L.; Combalbert, S.; Sournia-Saquet, A.; Mazarguil, H.; Faller, P. Redox Chemistry of Copper-Amyloid-beta: The Generation of Hydroxyl Radical in the Presence of Ascorbate is Linked to Redox-Potentials and Aggregation State. *ChemBioChem* **2007**, *8* (11), 1317–1325.
- (71) Jiang, D.; Men, L.; Wang, J.; Zhang, Y.; Chickenyen, S.; Wang, Y.; Zhou, F. Redox reactions of copper complexes formed with different beta-amyloid peptides and their neuropathological relevance. *Biochemistry* **2007**, *46* (32), 9270–9282.
- (72) Santoro, A.; Ewa Wezinfeld, N.; Vasak, M.; Bal, W.; Faller, P. Cysteine and glutathione trigger the Cu-Zn swap between Cu(II)-amyloid-beta4–16 peptide and Zn7-metallothionein-3. *Chem. Commun. (Cambridge, U. K.)* **2017**, *53*, 11634.
- (73) Misiti, F.; Clementi, M. E.; Giardina, B. Oxidation of methionine 35 reduces toxicity of the amyloid beta-peptide(1–42) in neuroblastoma cells (IMR-32) via enzyme methionine sulfoxide reductase A expression and function. *Neurochem. Int.* **2010**, *56* (4), 597–602.
- (74) Carelli-Alinovi, C.; Misiti, F. Methionine 35 sulfoxide reduces toxicity of A β in red blood cell. *Eur. J. Clin. Invest.* **2017**, *47* (4), 314–321.
- (75) Butterfield, D. A.; Sultana, R. Methionine-35 of A β (1–42): Importance for Oxidative Stress in Alzheimer Disease. *J. Amino Acids* **2011**, *2011*, 10.
- (76) Suprun, E. V.; Khmeleva, S. A.; Radko, S. P.; Kozin, S. A.; Archakov, A. I.; Shumyantseva, V. V. Direct electrochemical oxidation of amyloid- β peptides via tyrosine, histidine, and methionine residues. *Electrochem. Commun.* **2016**, *65*, 53–56.
- (77) Suprun, E. V.; Radko, S. P.; Khmeleva, S. A.; Mitkevich, V. A.; Archakov, A. I.; Makarov, A. A.; Shumyantseva, V. V. Electrochemical oxidation of amyloid-beta peptide isoforms on carbon screen printed electrodes. *Electrochem. Commun.* **2017**, *75*, 33–37.
- (78) Brabec, V.; Mornstein, V. Electrochemical behaviour of proteins at graphite electrodes: II. Electrooxidation of amino acids. *Biophys. Chem.* **1980**, *12* (2), 159–165.
- (79) Tsai, H.; Weber, S. G. Influence of tyrosine on the dual electrode electrochemical detection of copper(II)-peptide complexes. *Anal. Chem.* **1992**, *64* (23), 2897–2903.
- (80) Hanss, J.; Krüger, H.-J. The First Stable Copper(III) Complex Containing Aliphatic Thiolates as Ligands: Structural and Spectroscopic Evidence for CuII and CuIII Ions in Complexes with Square-Planar CuN2S2 Coordination Environments. *Angew. Chem., Int. Ed. Engl.* **1996**, *35* (23–24), 2827–2830.
- (81) Hoganson, C. W.; Babcock, G. T. Radical Chemistry of Histidine and Imidazole. In *Metal Ions in Biological Systems*, Sigel, H., Eds.; 1994; Vol. 30, pp 77–107.
- (82) Melnik, M.; Kabesova, M. Copper(III) coordination compounds: Classification and analysis of crystallographic and structural data. *J. Coord. Chem.* **2000**, *50* (3–4), 323–338.
- (83) Houghton, E. A.; Nicholas, K. M. In vitro reactive oxygen species production by histatins and copper(I,II). *JBIC, J. Biol. Inorg. Chem.* **2009**, *14* (2), 243–251.
- (84) Jin, Y.; Cowan, J. A. DNA Cleavage by Copper-ATCUN Complexes. Factors Influencing Cleavage Mechanism and Linearization of dsDNA. *J. Am. Chem. Soc.* **2005**, *127* (23), 8408–8415.
- (85) Brogden, K. A. Antimicrobial peptides: pore formers or metabolic inhibitors in bacteria? *Nat. Rev. Microbiol.* **2005**, *3* (3), 238–250.
- (86) Soscia, S. J.; Kirby, J. E.; Washicosky, K. J.; Tucker, S. M.; Ingelsson, M.; Hyman, B.; Burton, M. A.; Goldstein, L. E.; Duong, S.; Tanzi, R. E.; Moir, R. D. The Alzheimer's disease-associated amyloid beta-protein is an antimicrobial peptide. *PLoS One* **2010**, *5* (3), e9505.
- (87) Streltsov, V. A.; Varghese, J. N.; Masters, C. L.; Nuttall, S. D. Crystal structure of the amyloid-beta p3 fragment provides a model for oligomer formation in Alzheimer's disease. *J. Neurosci.* **2011**, *31* (4), 1419–26.
- (88) Kumar, D. K.; Choi, S. H.; Washicosky, K. J.; Eimer, W. A.; Tucker, S.; Ghofrani, J.; Lefkowitz, A.; McColl, G.; Goldstein, L. E.; Tanzi, R. E.; Moir, R. D. Amyloid-beta peptide protects against microbial infection in mouse and worm models of Alzheimer's disease. *Sci. Transl. Med.* **2016**, *8* (340), 340ra72.